Brigham Young University
BYU ScholarsArchive

All Theses and Dissertations

2018-12-01

The Design, Construction, and Thermal Diffusivity Measurements of the Fluorescent Scanning Thermal Microscope (FSTM)

Samuel Hunter Hayden
Brigham Young University

Follow this and additional works at: https://scholarsarchive.byu.edu/etd

 Part of the Mechanical Engineering Commons

BYU ScholarsArchive Citation

Hayden, Samuel Hunter, "The Design, Construction, and Thermal Diffusivity Measurements of the Fluorescent Scanning Thermal Microscope (FSTM)" (2018). *All Theses and Dissertations*. 7039.
https://scholarsarchive.byu.edu/etd/7039

This Thesis is brought to you for free and open access by BYU ScholarsArchive. It has been accepted for inclusion in All Theses and Dissertations by an authorized administrator of BYU ScholarsArchive. For more information, please contact scholarsarchive@byu.edu, ellen_amatangelo@byu.edu.

The Design, Construction, and Thermal Diffusivity Measurements of the Fluorescent Scanning Thermal Microscope (FSTM)

Samuel Hunter Hayden

A thesis submitted to the faculty of
Brigham Young University
in partial fulfillment of the requirements for the degree of

Master of Science

Troy R. Munro, Chair
Matthew R. Jones
Marc D. Killpack

Department of Mechanical Engineering

Brigham Young University

Copyright © 2018 Samuel Hunter Hayden

All Rights Reserved

ABSTRACT

The Design, Construction, and Thermal Diffusivity Measurements of the Fluorescent Scanning Thermal Microscope (FSTM)

Samuel Hunter Hayden
Department of Mechanical Engineering, BYU
Master of Science

Over the life of nuclear fuel, inhomogeneous structures develop, negatively impacting thermal properties. New fuels are under development, but require more accurate knowledge of how the properties change to model performance and determine safe operational conditions. Measurement systems capable of small–scale, pointwise thermal property measurements and low cost are necessary to measure these properties and integrate into hot cells where electronics are likely to fail during fuel investigation. This project develops a cheaper, smaller, and easily replaceable Fluorescent Scanning Thermal Microscope (FSTM) using the blue laser and focusing circuitry from an Xbox HD-DVD player. The FSTM also incorporates novel fluorescent thermometry methods to determine thermal diffusivity. The FSTM requires minimal sample preparation, does not require access to both sides of the sample, and components can be easily swapped out if damaged, as is likely in irradiated hot cells. Using the optical head from the Xbox for sensing temperature changes, an infrared laser diode provides periodic heating to the sample, and the blue laser induces fluorescence in Rhodamine B deposited on the sample's surface. Thermal properties are fit to modulated temperature models from the literature based on the phase delay response at different modulated heating frequencies. With the FSTM method, the thermal diffusivity of a 10 cent euro coin was found to be 21±5 mm^2/s. This value is compared to Laser Flash Analysis and a Thermal Conductivity Microscope (which used thermoreflectance a method), which found the thermal diffusivity to be 30.4±0.1 mm^2/s and 19±3 mm^2/s, respectively. The hardware and instrumentation performed as expected, but the property measurements show that the device is not yet optimized to provide accurate measurements with current heat transfer models. Future work is discussed to investigate the accuracy and necessary modeling adjustments, as well as refinements to the instrumentation.

Keywords: thermal diffusivity, fluorescent thermometry, photothermal, instrumentation

ACKNOWLEDGEMENTS

I would like to acknowledge the help of Dr. Troy Munro in teaching, mentoring, and advising me throughout my time as a graduate student. I am very grateful for the time he took to work with me and help me understand how to succeed. It was a challenging experience and Dr. Munro helped inspire confidence in myself and prepare me for what comes next. I would also like to acknowledge the incredible support of my wife, Eliza, who works extremely hard to help me concentrate on and enjoy my work, and I hope that my efforts also support her to the same degree. Our two kids, Elliot and Fiona, have also helped make life great. There are many other students that have helped contribute to this research and process of making it through graduate school. Ryker Haddock, Greg Bird, Spencer Diehl, Turner Palombo, Kegasi Turbovsky, and Sam Hales have all contributed to the success and enjoyment of the project. Derek Sanchez and Peter Hartvigsen, fellow TEMP lab students, have been great friends and associates to study and work with, I would like to acknowledge the comradery that they have brought to the lab.

I would also like to acknowledge the funding from the Office of Graduate Studies to work on this project and help undergraduates contribute to the project. The help of Zhourui Song, Zilong Hua, and David Hurley is much appreciated to get the LFA and TCM measurements.

TABLE OF CONTENTS

LIST OF TABLES

LIST OF FIGURES

1 INTRODUCTION

1.1 Motivation

To help nuclear reactors be more accident tolerant, there is a need for thermal property measurements of new materials, especially nuclear fuels. Nuclear fuel pellets are roughly 15 millimeters wide and can experience a temperature difference of hundreds of degrees Kelvin from the center to the outer surface [3]. By the end of fuel's life (high burn-up), non-homogeneous microstructures form, causing hot spots and reducing heat transfer to the coolant. New accident tolerant fuels are in development [4] that have improved thermal conductivity and thermal diffusivity, but it is necessary to understand how their properties change over time to accurately model their performance and determine safe operational conditions. More accurate models of the thermal property distribution mean better predictive modeling. Understanding and predicting the fission of radioactive elements and the effect of their distribution in the fuel helps prepare for adequately cooling the fuel and keeping the reaction under control. If power generation becomes uncontrolled, the reactor may become unstable and lead to the destruction of the containment structure and release of harmful radiation to the surrounding area. Accidents in nuclear power plants can have severe and long lasting consequences. Under accident conditions, heat concentrations due to inhomogeneous material may cause the fuel rods to overheat unpredictably [5]. Spent fuel with these heat concentrations can be analyzed to learn more about how the thermal properties developed in the fuel. Current thermal property measurement systems are limited in

spatial resolution, cost, and do not integrate well into containment shelters shielded against radiation, called hot cells (where electronics have a higher failure rate), for fuel investigation during Post Irradiation Examination (PIE). The ultimate impact of this work is to attempt to maintain nuclear safety with a much cheaper, smaller, and more easily replaceable device based on the laser assembly from an Xbox to measure nuclear materials during PIE.

Thermal characterization, is important for predicting the behavior of materials in a variety of applications. This project focuses on nuclear fuel, but other topics where knowledge of these properties is important include combustion and energy generation. In these cases, the material properties affect the efficiency, longevity, and safety of the process. In a gas turbine, engine efficiency increases as the operating temperature goes up. Knowing the thermal properties of the materials involved is key in improving these generation methods. When analyzing nuclear fuel that experiences large temperature gradients over a small distance, the thermal conductivity at each location determines the heat spread and distribution through the material. In such a complex process it is important to know how the material will behave, understanding and predicting this better can increase the safety of the process. The purpose of our sensor is to collect thermal property data on nuclear fuel at various stages of use.

Current limitations of thermal conductivity measuring methods such as 3ω [6], laser flash [7], and laser reflectance [8] in determining the properties of these fuels include:

- High cost of replacing components damaged in a radioactive examination environment
- Inadequate spatial resolution
- Difficult sample preparation
- Incapability of measuring rough surfaces
- Low portability and large volume of equipment

- Difficulty of switching out damaged components remotely
- Cost of current sensors

Creating a measurement system that can overcome the bulleted limitations will make it easier to analyze nuclear fuels and contribute to the data required to predict their behavior. To address these difficulties, we propose to design, build, and test a sensor based on a commercially available Blu-ray player to provide spatially resolved measurements of thermal properties. We will make this thermal property instrument from a modified Blu-ray player to both sense and induce temperature changes in the materials at a fraction of the cost of other thermal characterization instruments. The motors in the Blu-ray player are also capable of the fine motor control required to resolve these fine-scale properties. An inexpensive infrared laser diode (780nm) provides periodic heating to the sample, and the blue laser in the Xbox optical head induces fluorescence in fluorescent dye on the sample's surface. A photodiode captures the emitted fluorescent light, and a lock-in amplifier outputs the phase delay between heating and fluorescing for analysis in the frequency domain heat diffusion equation to determine the thermal diffusivity of the sample.

1.2 Background

1.2.1 How Nuclear Fuel Changes Over Lifetime

Certain nuclear fuels, like U_3Si_2, show disagreements on experimentally collected data of thermal properties [9]. One reason for this is the presence of significant impurity phases, requiring more accurate analysis of how the thermal properties change over a range of temperatures and manufacturing processes. It takes significant effort to analyze the data of these materials to get sufficient data for capturing steady state operation conditions and design basis accident scenarios [9]. There are many factors that contribute to changes in a fuel over its lifetime. Three of these

factors include fission product migration and swelling, pellet clad interaction, and restructuring [2]. Restructuring is shown in the bottom left quadrant of Figure 1-1, along with the other occurrences during the burn up lifetime. Fission products are atoms that appear in place of the heavy-metal atom, and some of them become free to chemically attack the cladding material around the fuel. Additionally, as the heavy-metal atoms are replaced, dimensional changes occur as the fuel swells. Due to steep temperature gradients, these fission products can also migrate away from the region where they are formed. Pressures of expanding gases may develop and the vapors may also condense in cooler regions of the fuel element. Due to sharp temperature distributions, the fuel pellet changes shape, causing it to interact with the cladding and increase stresses. The fuel develops an hourglass shape due to a switch from plane-strain in the mid-plane to plane-stress at the upper and lower faces. If the fuel is pressed against the cladding it can result in failure by embrittlement or stress cracking. Pellet clad interaction (PCI) is a major source of cladding failure. Restructuring of the fuel includes radial redistribution of component elements and substantial swelling due to movement of insoluble fission gasses. This is also caused by the high temperatures and gradients in the fuel. This restructuring results in the formation of a central hole Figure 1-1 columnar grains, and substantial grain growth just outside the columnar grain region. These columns form along the direction of the thermal gradient. The temperature difference in oxide fuels between the centerline and external surface can exceed 1000K over a small distance [2]. All of these changes affect the thermal conductivity of the material. The thermal conductivity tends to decreases, meaning heat does not leave the material as well and may result in hot spots [10]. This project focuses on the work to characterize this local thermal conductivity degradation in other samples in preparation for nuclear fuels.

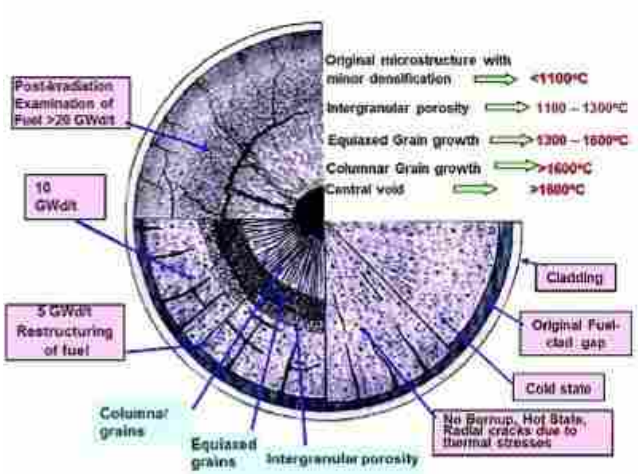

Figure 1-1: Stages of fuel material over its lifetime. With increasing time and temperature, the material changes as shown in [2].

1.2.2 Other Thermal Characterization Methods

There are many other methods for analyzing thermal properties of materials. Bulk property measurements fall under the category of thermal parameter identification methods (a common example of this is explained in the Laser Flash section below). Finer resolution measurements are related to thermal topography. Topography indicates generating a map of the thermal properties at each point of the sample's surface, which is the proposed function of the FSTM. An overview of these methods is presented here to understand the advancements that have been made in the field. The methods reviewed include foundational techniques for bulk property measurement, time domain methods, microscopic resolution, frequency domain methods, and methods that make use of fluorescence in the temperature measurements.

Laser Flash

A foundational work in property determination was by Parker et al [7], in which how light pulses absorbed by a specimen can be analyzed at the opposite surface to determine the thermal properties based on the delay between the temperature signals on either side of the sample. The

samples analyzed with this method were coated with camphor black to maximize absorption and ensure that the sample was heated uniformly. This method overcame difficulties of previous methods when dealing with heater source and sink contact resistances. The sample was heated, and the temperature rise on the opposite side was recorded via thermocouple. Recent versions of this method use high speed IR sensors and improve modeling by considering subsurface light absorption and radiation effects. This temperature response is modeled as the response to an instantly absorbed pulse. Heat diffusion models for a thermally insulated and uniformly thick solid relate the thermal diffusivity to the time it takes the heat pulse to heat the back surface of the sample to half the maximum temperature rise. The resulting expression for thermal diffusivity is

$$\alpha = \left(\frac{1.38L^2}{\pi^2 t_{\frac{1}{2}}} \right) \tag{1}$$

where L represents the thickness of the sample and $t_{\frac{1}{2}}$ represents the time for the back surface to meet half its maximum temperature rise. There are multiple assumptions in the LFA model, pointed out in [11], and they also affect the experimental setup for this method, shown in Figure 1-2. The LFA model assumes one dimensional heat transfer, meaning the laser pulse width must be sufficiently short to be considered negligible in comparison to characteristic time of the heat diffusion process. Uniform heating is necessary on the front of the sample, and the sample must be adiabatically insulated, homogeneous, and have a uniform geometry. The losses from the surface are also neglected for the most basic models. This technique, combined with differential scanning calorimetry and dilatometry, has been favored by the nuclear industry to measure the thermal conductivity of fuels where $k = \alpha/\rho c_p$ [12], with k representing the thermal conductivity, α the thermal diffusivity, c_p the specific heat, and ρ represents the density. It is a proven method for parameter identification of the bulk thermal diffusivity of a material. Other methods will be

examined that are capable of determining how the property varies spatially across the sample. This method also cannot explicitly account for multiple layers of material on the sample.

Scanning Thermal Microscopy (SThM)

Non-contact scanning thermal microscopy, introduced in [13], overcomes the challenge of

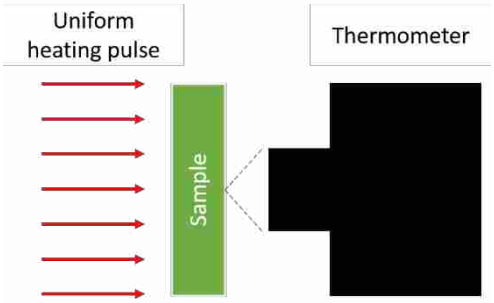

Figure 1-2: Experimental set-up for laser flash.

uncertainty due to contact resistance in previously developed methods. The SThM method can probe local thermal diffusivity with 2-3 μm resolution. This method uses quasiballistic air conduction across a 10-100 nm air gap between a heated microprobe and the sample. This heating set up is shown in Figure 1-3. A thin wire is exposed close to the surface of the sample, heated, and the thermal diffusivity is found by fitting the effective thermal resistance to a heat transfer model like the one developed in [14]. The model includes microprobe conduction, convective losses, and radiative losses. This method has a fine spatial resolution but requires calibration to determine the tip to sample thermal conductance and radius using multiple reference samples. The results in [13] are within 5%-10% of steady-state methods and theoretical models, which can be improved with frequency-based wire heating [15].

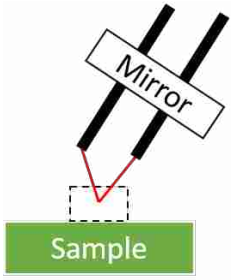

Figure 1-3: Heating method for STM methods.

3ω Method

The 3ω method is an AC technique (based on analysis in the frequency domain) of measuring thermal properties [6, 7, 16, 17]. When first published, this method overcame common problems due to sensitivity to black body radiation. This sensitivity was no longer a problem because the samples were very thin compared to samples where sensitivity to black body radiation had a larger effect [6]. The 3ω method involves applying a current controlled sinusoidal heating of a metal layer deposited onto a surface (Figure 1-4) at 1ω and locking into the 3ω voltage response. 1ω represents the frequency of the heating wave and 3ω is three times that frequency, which corresponds to the desired response. In the 3 ω method, it is required to know dR/dT, the slope of the average resistance as a function of temperature, to determine k. The amplitude and phase are measured over a range of frequencies [18]. Where time domain methods measure the time to a certain temperature, this method analyzes the temperature responses in the frequency domain.

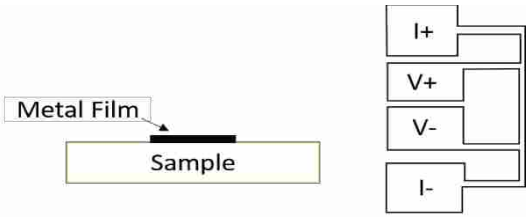

Figure 1-4: Schematic of metal film heating element (a). Possible shape for heating pads and voltage sensing (b).

Sample preparation can involve polishing the surface to a near mirror finish or ultrasonic cleaning in acetone. This is then followed by lithographic deposition of the thin metallic heater. This is because it is necessary to lay a pattern of pads for joule heating and voltage measurements. This method is good for high temperature measurements done up to 750K [6], and compared to others the time for equilibration is much shorter, just a couple oscillations of the heating element. This method has been successfully applied to fresh nuclear fuels [19], but not irradiated samples

because of the expected effect radiation damage will have on the metallic heater. Additional, the ability to provide spatially resolved measurements is not possible.

Thermoreflectance Methods

Thermoreflectance methods can be analyzed in the time or frequency domain [8, 20-22]. These methods involve a modulated heating (pump) laser to heat a sample and a sensing (probe) laser reflected off the sample's surface into an optical detector. The path of this light and the electrical connections are shown in Figure 1-5. The surface of the sample is heated via laser, and as the surface temperature changes, so does the reflectance. Reflected light that varies with temperature is collected by a photodiode.

The Frequency Domain Thermoreflectance (FDTR) method [21] is another frequency domain method that measures the changing reflectance, where the amplitude and phase lag are measured in comparison to the heating signal. The properties can then be determined by fitting the resulting data to the appropriate frequency domain model of the heat equation [11]. This method uses a lock-in amplifier to collect the amplitude and phase response data of the reflected beam. Because the phase delay also contains the delay due to cables and instruments, the work presented in [21] splits a portion of the pump laser light to be sent to an identical photodetector and is used as the reference for the lock-in amplifier. This reference signal is valid as long as the sum of the path that the light travels is the same as that of the reflected probe beam detector. The time domain version of thermoreflectance methods also use a pump and probe laser set up, but a transient temperature change is measured, instead of the phase delay of a modulated signal. The time domain method requires complex instrumentation, including high speed pulsed lasers and complex optical table set-ups. This method is used at the Idaho National Laboratory with their Thermal Conductivity Microscope (TCM) for property measurements [23]. One shortcoming of this method

is the necessity of a mirror like finish and adding a highly reflective material to the samples surface to ensure adequate reflection of the probe laser. While this removes the surface structure of the sample, it acts as a reference value to determine the thermal conductivity.

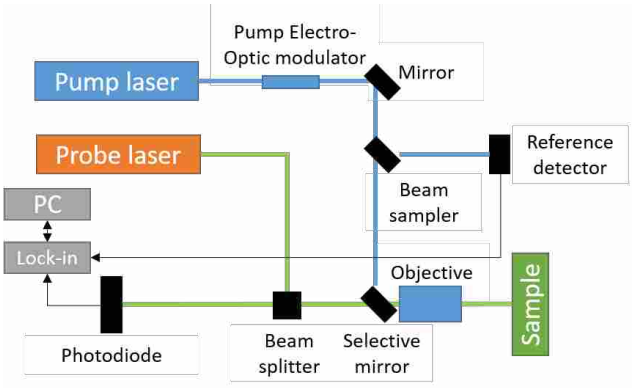

Figure 1-5: Experimental set-up for FDTR. This schematic shows the pump and probe lasers, optics for directing the lasers to the sample, and the photodiode and lock in for collecting and analyzing the signal.

Thermal Conductivity Microscope (TCM)

The Thermal Conductivity Microscope was invented an Idaho National Labs and is designed to simultaneously measure local thermal diffusivity and conductivity [24]. The device continuously heats a sample with a modulated laser beam, and the relates the temperature response is related to a reflected optical signal (shown in Figure 1-6). Based on temperature induced changes in reflectivity, the thermal properties can be inferred. The sample is coated with a thin layer of gold to ensure strong optical absorption, and also establish a boundary condition that contains the sample's thermal conductivity. The data of interest is the phase lag of the reflected light of the probe beam as its distance from the pump heating spot is changed. The phase lag increases as the probe laser moves away from the location of heating, and the slope of the phase profile can be related to the thermal properties.

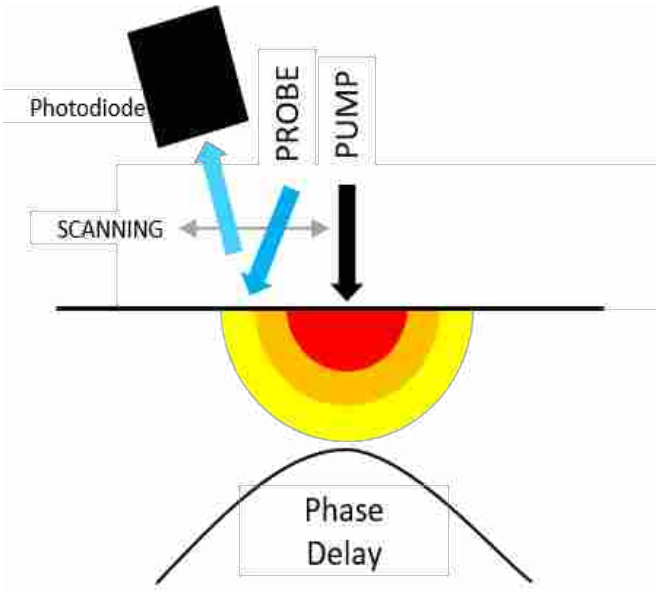

Figure 1-6: Method of scanning the probe laser to find the phase delay at a spatial distance from the pump heating spot, the phase delay increases in magnitude as the probe scans away from the center

Heterodyne Picosecond Thermoreflectance

The heterodyne picosecond thermoreflectance (HPTR) method eliminates errors and artifacts in the signal to be analyzed, such as background noise and misalignment of pump and probe beams. To fix these issues, this method uses two pump and probe lasers at slightly different modulation frequencies. This frequency offset is shown in Figure 1-7 where the pump is modulated at 76 MHz and the probe at 76.006 MHz. The heterodyning method is a way to extract data that is represented in the modulated frequency of the signal. The particular method referenced was developed for multi-layer samples. The modeling developed in [25] makes four major assumptions. These include a pump duration that is much shorter than the scale of the experiment, cylindrical symmetry of the temperature field, uniform temperature variation within the deposited metal layer on the surface, and that the substrate is a semi-infinite medium. The use of multiple, large Ti. Sapphire lasers, and the remaining optics are not easily integrated into a hot cell environment.

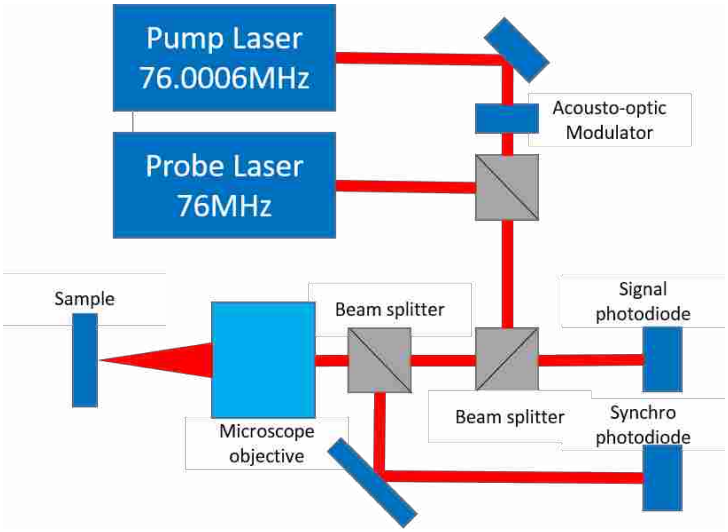

Figure 1-7: Heterodyne system experimental set-up.

Micro-Photoluminescence Spectroscopy

In reviewing the literature on non-contact measurements of thermal properties, one particular source was mentioned in [11] to have used fluorescence. This method is presented in [26] and presents measurements on individual nanowires with temperature dependent micro-photoluminescence spectroscopy. This work sought to advance understanding of thermal transport in low-dimensional materials. A 405nm laser was used to simultaneously heat and excite fluorescence in the sample, shown in Figure 1-8. Spectra were captured at different temperatures and the modeled heat conduction through a solid rod of given cross section was analyzed to determine the thermal conductivity of the nanowires. Radiative heat loss was ignored because when quantified at its peak, it was much smaller than the heat flow due to conduction through the wire. This is relevant to this FSTM project because conduction is the main source of heat transfer in the samples that each method measures. Other methods have used fluorescence to successfully analyze spider silk thermal properties [27].

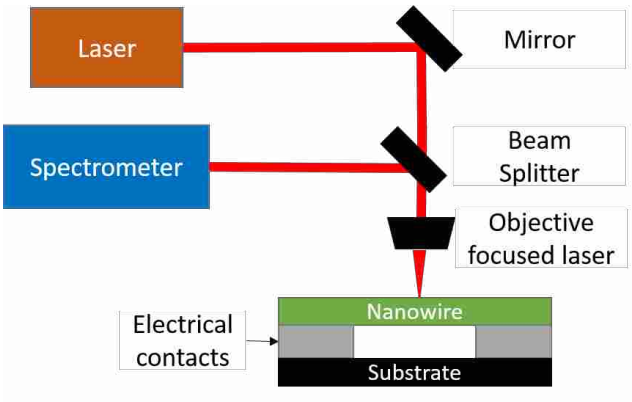

Figure 1-8: Micro-photoluminescence spectroscopy experimental set-up.

1.2.3 Principles of Fluorescence

A novel aspect of the FSTM is the use of fluorescent thermometry. The following is a general overview of fluorescence and its defining characteristics. When an electron is excited into a higher energy state by a shorter wavelength (and hence higher energy) light, its return to the ground-state orbital results in the emission of a photon. One characteristic of the fluorescent process is that the emitted photon is at a longer wavelength than the exciting light because of vibrational losses of the electron. This longer wavelength light can be related to temperature for non-destructive thermometry measurements because of the relationship between increased temperature and more vibrational energy losses [15]. This difference in wavelength between absorption and emission is called the Stokes Shift, and is evident on absorption and emission graphs for fluorescent dyes as seen in Figure 1-9.

Another interesting property of fluorescence is that the emission wavelength is independent of the excitation wavelength, known as Kasha's rule [28]. This is useful when a particular emission wavelength is necessary, because any probe laser of higher energy could excite it, though there is usually an excitation wavelength that will result in the highest quantum yield of emission. This is apparent in Figure 1-9 where a peak in emission is evident.

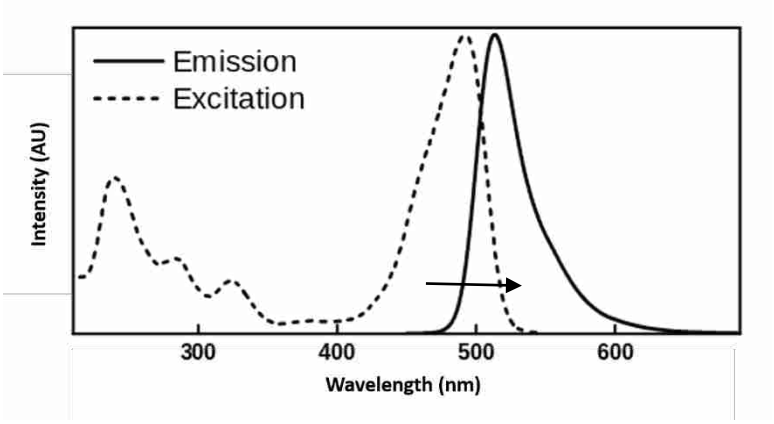

Figure 1-9: Example of Stoke's Shift, where the emission peak is at a higher wavelength than the absorption peak, shown by the arrows. This difference in wavelengths is different for each dye [1]. Image source: Wikipedia Commons, User: Zadelrob under a Creative Commons license.

These methods of relating the emission to temperature have been successfully used to measure the thermal diffusivity of thin fibers and glycol [16]. Relating temperature in measurements when heat input is by light fall under the broad umbrella of photothermal techniques.

1.2.4 Fluorophores: Rhodamine B vs. Quantum Dots

Two options for the fluorescent dye include Rhodamine B and quantum dots. Within the group of inorganic fluorophores, quantum dots are of interest due to their stability and ease of application to a surface. Quantum dots are inorganic nanocrystals with a variety of useful applications. Due to their unique properties it is possible to synthesize particles with a tunable light emission. Their photoluminescent properties mean that as they absorb photons of light, electrons are excited to a higher state and a photon is emitted as the electron returns to its original state. By adjusting the size of the quantum dots, which range from 2 – 10 nm, fluorescent emission can be chosen between 400 and 4000 nm [29].

In addition to inorganic quantum dots as a fluorescent dye, there are organic dyes that exhibit similar photoluminescent properties. One prominent example is Rhodamine B (RhB). Rhodamines are a fluorophore, that when synthesized into a dye exhibit fluorescent emission with

temperature dependent intensity. As the temperature increases, the intensity of fluorescent emission decreases. This is shown in Figure 1-10 where the RhB data was collected on the emission spectra of fluorescent dye heated by the pump laser. Organic dyes have a smaller separation between the absorption and emission spectrum than QDs [30]. When comparing the two, it is notable that quantum dots have increased absorption as the excitation energy increases (shorter wavelengths). QDs also have a much higher quantum yield when emitting in the near infrared wavelength region. Quantum dots are more expensive, but have a larger selection of excitation and emission wavelengths and are more stable over time [31].

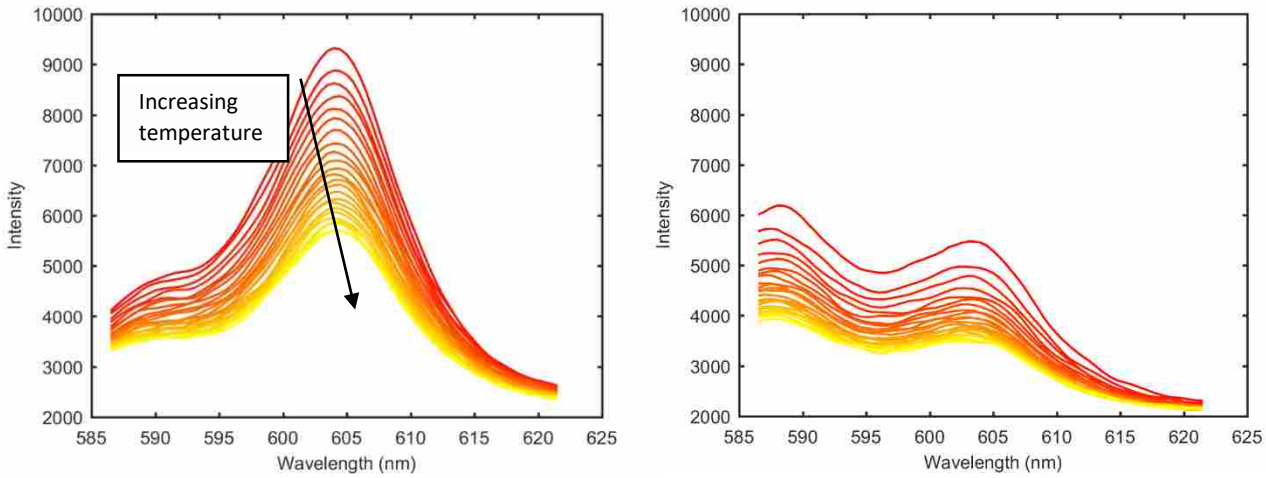

Figure 1-10: Rhodamine B emission intensity over a 25 second heating period (left) and Quantum dot emission over the same period of time (right). The trend of decreasing intensity with increasing temperature is evident as the sample was heated by the laser.

Other works present the utility of RhB in varied applications. RhB has been used as a non-reactive sensor in biological systems [32] and in determining the thermal conductivity of carbon nanotubes [33]. To help select a fluorophore for use with nuclear fuel, RhB has been found to react with the uranyl ion in acidic solutions rather than the UO_2 compound found in nuclear fuel [34].

1.3 Contributions of the Current Work to the State-of-the-Art

While the methods discussed in the previous section are dependable and well established, laser flash is limited to finding bulk properties, while the other five are based on equipment that is expensive, not suited for use in a highly radioactive environment that causes electronics failure [35] and optical browning, or may require lengthy sample preparation procedures like polishing the samples. This poses problems if the surface of the sample should be preserved. Additionally, the other methods that employ the use of fluorescence have been performed on nanowires, spider silk, and glycol, which have very different geometric and material properties than nuclear fuels. The analysis of different geometries and properties will contribute to the variety of scenarios that fluorescent photothermal methods have been tested and analyzed. Additionally, this method will examine point wise properties, instead of bulk, which have not been examined in depth in other fluorescent methods.

In addition to the methodology involved, this project contributes new instrumentation for thermal property determination experiments that will advance the state-of-the-art methods. The PHR-803t is an inexpensive laser assembly that comes out of an Xbox Blu-ray player. It contains lasers, lenses and a focusing system and is readily available. This compact optical head reduces the amount of engineering and cost of the FSTM. It contains the circuitry and components necessary for focusing the laser, inducing fluorescence, and holding the heating laser, all in a compact and easily replaceable unit. Its use was inspired by open source software and circuit boards worked on by hobbyists and hackers. The most prominent example of controlling the circuitry of the device was accomplished by [36] for the purpose of making a circuit board printer. The methods of controlling the focusing fixture and laser diodes in the PHR are proprietary to DVD player manufacturers, but the circuitry was reverse engineered and the circuit board in Appendix A was developed to control the lasers and focusing built into the PHR. The focus of the

current project seeks to refine the optical control of the PHR-803t and contribute a useful instrument to nuclear fuel and thermal property analysis. This project also contributes to more affordable and simple nuclear fuel analysis. Because of the irradiated environment that these types of measurements take place in that cause electronics to fail, device replacement can be costly. Because the PHR-803t has many of the electronics self-contained, when device failure arises, the optical head can be swapped out with minor cost consequences. This will make fuel analysis more feasible by simplifying the process when parts fail and lowering the cost. This thesis is limited to validate the performance of this device in measuring thermal diffusivity of a solid material. Future work will use the device to understand how nuclear fuel will perform in a reactor. This specific project is to use a working sensor to take data on materials of known thermal diffusivity measured with standard techniques.

The FSTM device presented in this thesis uses fluorescent thermometry to measure pointwise properties. This is a well-developed temperature sensing method for use with thermometry techniques [30, 31, 37], and requires a dye, short wavelength laser, and photo-sensor. To sense the temperature of a spent fuel or calibration sample, a fluorescent dye needs to be deposited on the surface of the sample. This dye emits a specific spectrum of light that varies with temperature when excited with the blue laser. Two options for the fluorescent dye include Rhodamine B and quantum dots.

Like the FDTR method, this device involves a modulated pump laser to heat a sample, but instead of a probe laser being reflected into an optical detector, the fluorescent dye is excited by a probe laser for temperature variation detection by a photodiode. Similar to the frequency domain methods discussed previously in literature review, the FSTM uses a lock-in amplifier to analyze the modulated light data from the amplified photodiode. The FSTM also heats samples via infrared

laser. In laser flash analysis, the temperature changes are sensed by infrared camera, and in 3ω by the heating pads. The FSTM method shares certain characteristics with some other methods, and combines them into a unique system.

The information in Table 1-1 presents a comparison of the performance of laser flash, thermal conductivity microscope (TCM), and a heterodyne laser system to the FSTM. At 1μm optical resolution the fluorescent Blu-ray method is comparable to the TCM, finer than the 2-6μm of the Heterodyne System. The laser flash resolution is not a relevant measure of comparison, as it is used for bulk parameter identification and not mapping spatially varying properties. However, because laser flash analysis (LFA) is the primary method of analyzing nuclear fuels, we include it in some of our comparisons. The major advantage of the Blu-ray system is the size and cost. It is under a thousand dollars while others range from $20-130k. Additionally the experimental set up takes up less than half the volume of the next smallest set up, which is the LFA. These systems are compared in Table 1-1.

Table 1-1. Comparison of thermal property characterization methods

	LASER FLASH (LFA)	*TCM*	*HETERODYNE LASER SYSTEM*	*FSTM*
SIZE	22 x 21 x 34 cm	56 x 20 x 25 cm	~100 x 50 x 25 cm	25 x 18 x 15 cm
COST	$100k+	$20-30k	~$130k	<$10k
UNCERTAINTY	~5-10% [11]	~10% [11]	~10-15% [11]	~5-15% [38] previous fluorescent systems
RESOLUTION	N/A	Laser spot size 1 μm Thermal wave size ~50 μm	2-6 μm	Laser spot size 0.6 μm

This project seeks to advance the area of non-destructive thermal property measurements. An overview of the field in [11] discusses many non-contact methods, with only one mention of fluorescence in 200 references cited. These fluorescence methods have been limited to micro-photoluminescence spectroscopy that analyzes nanowire. While fluorescent thermometry is well

established in many applications, this project refines a novel use of fluorescent thermometry to contribute to the field of non-destructive property measurements. The advantages of this include simple sample preparation, non-destructive heating and data collection, requires access to only one side of sample, preserves surface structure of sample to be analyzed, and low cost components for temperature sensing. Another contribution of this project is the use of commercially available optical heads as a device for scientific measurements.

2 RESEARCH OBJECTIVES

The objectives of this project can be broken up into the following main tasks. These are:

- Assemble circuitry to control PHR-803t lasers and focus them, and use it to develop a modulated laser heating system.
- Collect fluorescent emission data emitted from sample's surface with the FSTM.
- Determine suitability of PHR's built in motors for use in moving the sample for pointwise measurements
- Use appropriate mathematical models to extract the thermal diffusivity from the acquired data.
- Determine the capability of the device to measure thermal properties samples of known and unknown material composition and properties.

3 EXPERIMENTAL SET-UP AND METHODS

This chapter will describe the construction of the FSTM. The FSTM consisted of three major subsystems: the optical head, the photodiode, and the lock-in amplifier. Figure 3-1 shows the system and various light signals traveling within it. The signal starts in the bottom left as it leaves the function generator and travels to the infrared laser and the lock-in amplifier. It sinusoidally modulates the intensity of the infrared lasers and functions as the lock-in's reference to compare with the fluorescence (induced by the blue laser) from the dye. The sample, on the bottom right of the figure, is heated by the infrared laser and emits the fluorescent signal up through

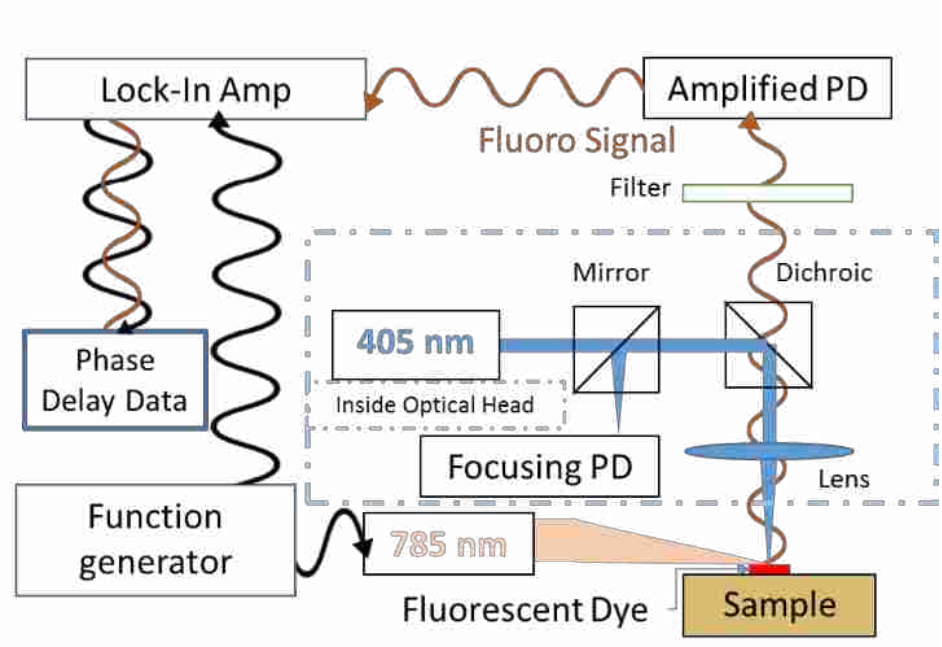

Figure 3-1: Block diagram of experimental set up. This diagram shows the components of the optical head, and the path of the fluorescent signal from the sample, to the photodiode, and then to the lock-in where it is compared to the reference and the phase delay

the PHR. The fluorescence is generated by the blue 405nm laser in the center of the figure that travels from the diode and through mirrors and lenses down to the sample. The signal from the sample and the other light travels up through optical filters and into the amplified photodiode. This modulated signal leaves the photodiode and goes to the lock-in amplified where it is compared to the reference, the phase delay is calculated, and sent to the computer via GPIO. The laser PHR is controlled through a special driver board designed by Diyouware [36] that receives signals from

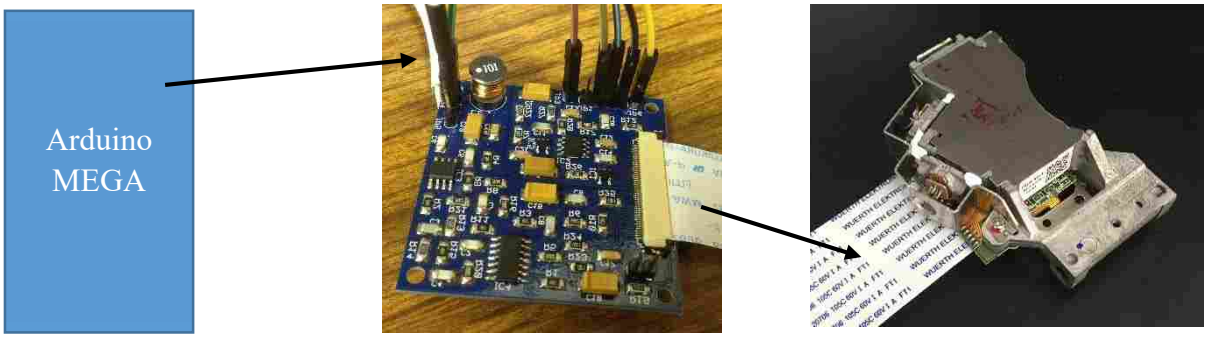

Figure 3-2: Overview of laser control electronics. The commands are sent via Arduino (left), through the driver board (middle) then through the FFC cable to the PHR (right).

an Arduino MEGA coded to turn on the lasers, start the focusing algorithm, and process the focusing signal coming back from the PHR. These three components are shown in Figure 3-2 and discussed in detail in the following chapter sections. Arduino code is given in Appendix D.

3.1 Laser Control Assembly and Troubleshooting

A PHR-803t optical head was used as the laser assembly for the FSTM. The PHR-803t laser assembly is from an Xbox 360 and it houses three laser diodes. The wavelengths of the laser diodes are 405nm, 680nm, and 780nm. The benefits of this optical component include the low cost (ease of replacement if damaged during use), tightly integrated optics, and focusing capability, the components for these functions are pointed out in Figure 3-3. It is connected to the control circuitry by a flex cable connected to the built in flexible flat cable (FFC) adapter, from which it can be easily separated and replaced. Two lasers are necessary for the fluorescent thermometry, one to

heat the sample (pump) and one to induce fluorescence (probe) in a fluorescent dye deposited on the sample.

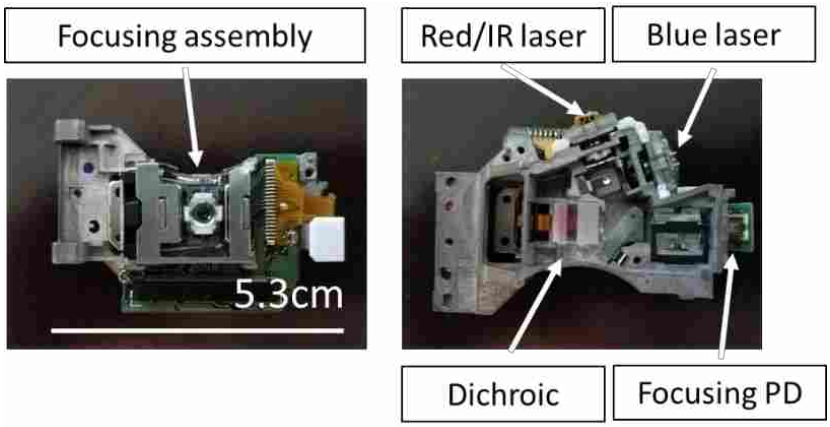

Figure 3-3: Close up image of PHR laser assembly. Features of interest include the locations for multiple lasers, the dichroic for directing each laser down through the bottom of the assembly, and the built in focusing photodiode for focusing the laser

Because the PHR-803t's built in laser driver (ATMEL ATR0885) can only turn on only one of the three lasers at a time, the blue laser is powered directly through the diode's anode and cathode using a constant current regulator that holds the current at ~85mA. A waveform generator (Agilent 33220A) outputs a sinusoidal signal that varied the amplitude of the heating laser by controlling the current through the diode. Because the IR laser in the PHR-803t was very low power (~10 mW), it did not heat the surface enough to produce detectable temperature fluctuations and an IR laser external to the PHR-803t was used. The data presented was collected with an external heating laser (785nm, 90mW) directed at the sample, aligned concentrically with the probe laser spot. Future devices will use a diode held in the position of the original diode by a 3D printed assembly. The infrared laser spot was centered over the blue laser spot and kept at such a distance that the infrared laser spot was larger than the blue so that the area of fluorescence was evenly heated by the beam, to allow for the assumption of 1D heating.

3.1.1 Circuit Board Assembly and Troubleshooting

The driver board designed by Diyouware [36] handles the signals that move between the Arduino and PHR in either direction. From the Arduino the commands are sent to turn lasers on or off and adjust their power. The driver board also processes a PWM signal from the Arduino to move the focusing lens up and down. The PHR also sends the focusing signal from its photodiode through the driver board where its components are combined, filtered and combined again before being read by the Arduino. Assembling the driver board stenciling solder paste onto the circuit board, placing the correct components according to Diyouware's instructions, and reflow soldering it in a reflow oven. The FFC connector, shown in Figure 3-4, often had solder bridges between multiple pins after the reflow heating process, and it was necessary to remove them afterwards with either a solder vacuum or solder wick. This problem was very difficult to overcome and the circuitry was transferred to a breadboard, sacrificing compactness, but making it easier to build the circuit section by section and solve problems as they arose. This made it possible to isolate issues and build a functioning circuit.

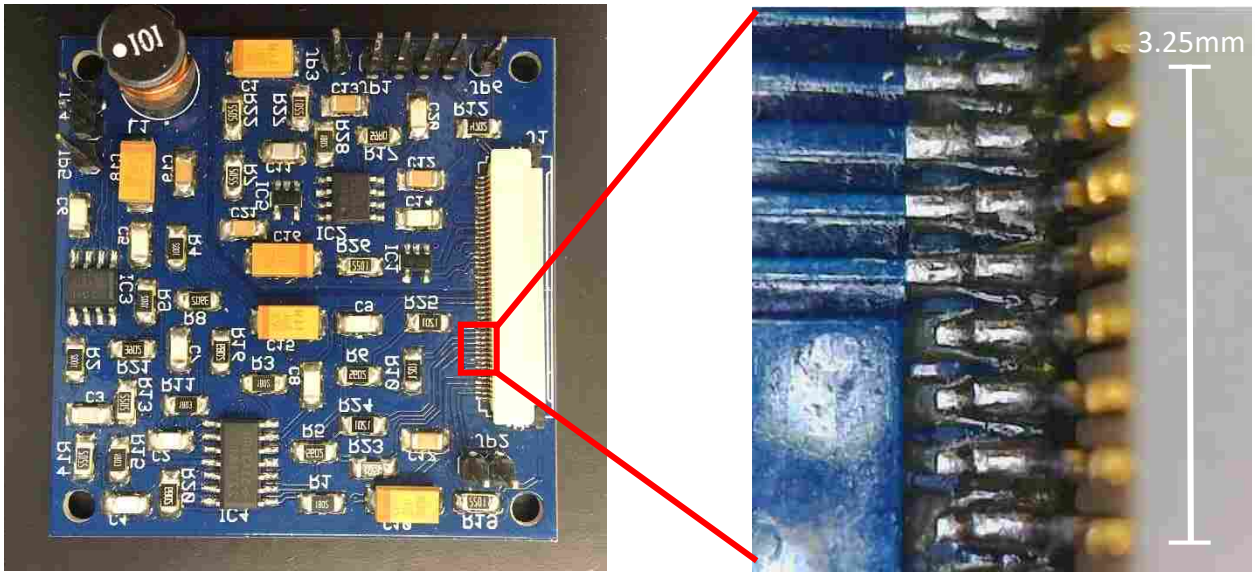

Figure 3-4: PCB designed by Diyouware and built by hand after extensive troubleshooting. Solder bridges between the small pins shown in the magnified area on the FFC connector, was the most common issue stopping the focusing from working.

3.1.2 Focusing Photodiode Troubleshooting

Until the circuitry was transferred to the breadboard, the lasers were able to be turned on and off, but the focusing did not work. Making more boards resulted in the same error and the problem could not be found. The signal from the focusing photodiode could not be measured with the oscilloscope and led to in depth troubleshooting to see where the focus error signal was being lost. The focusing photodiode has four quadrants that collect reflected light, when two quadrants are summed and subtracted from the other two the result equals zero when the laser is focused, meaning equal amounts of light are hitting each segment. But this signal did not transfer through the intermediate components and could not be measured at the output. One possible reason frequently mentioned by the designers of the circuit was noise. To eliminate noise, the ground lines between the digital and analog parts of the control circuit were isolated and grounded separately with a shielded cable on the cable that carried the focusing signal from the laser assembly to the Arduino in order to reduce the noise. The issue was eventually narrowed down to the small solder connections on the FFC cable adapter where solder bridges were frequent and nearly impossible to remove. On the boards where the solder bridges were removable the focusing worked, moving it to a breadboard eliminated this issue. To address the issue and still be able to use the compact PCB, the eagle source files were edited to increase the pad size for the FFC connector solder points. As shown in Figure 3-5 on the right, the pads on the customized PCB are wider and more consistent.

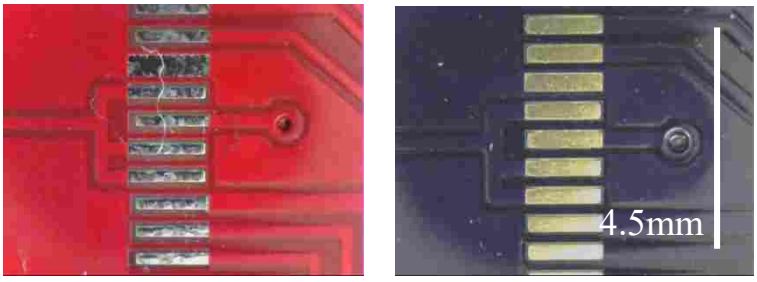

Figure 3-5: Image of original Diyouware PCB (left) and customized PCB (right). The pads on the updated version are bigger and more consistent.

3.2 Internal Photodiode

To take advantage of the tightly integrated optics of the PHR laser assembly, the initial plan was to use the focusing photodiode to focus the laser and also collect data on the intensity of the sample's emitted fluorescent light. Reading the documentation for the focusing photodiode (Melexis MLX75012, Figure 3-6), the SW1 and SW2 were identified as the pins that changed the sensitivity of the detector. These pins were located by disassembling one of the laser assembly photodiode's and tracing the pins (shown in the bottom middle of Figure 3-6) to the end of the flex cable through the small electrical traces in the bottom middle image of Figure 3-6. The orientation was verified by checking the pins that were already connected to the Diyouware driver board, it was then necessary to identify the other ones. The data sheet was then used to trace each pin back to its corresponding flex cable wire by following the PCB traces and vias shown in Figure 3-6 and using a multimeter to check continuity between pins and flex cable connection points. Once traced to the flex cable it was possible to probe them with an oscilloscope and measure the voltage response to light input. With the pins identified, it was noted that they were receiving 4.2 volts, meaning that the photodiode was already at maximum sensitivity, shown by the settings in the data sheet segment of Figure 3-6. Examining the output of the focusing photodiode under multiple conditions it was determined that the photodiode only outputs a signal when the laser focuses. Otherwise the signal is constant and could not be related to light intensity, because of this we chose a Thorlabs PDA36A amplified Si photodiode for fluorescent detection, while the internal photodiode would be used only for focusing. The Thorlabs detector was selected because it is designed for light detection between 350nm-1100nm, has 8 selectable gains in 10dB steps, and is easily mounted using Thorlabs mounting accessories. The photodiode and laser set-up is shown in Figure 3-8.

HD-DVD / Blu-Ray® / DVD Mode (SW0 = H) Detector-Pattern 1														
Gain Mode			A, B, C, D				E, F, G, H				RFP / RFN			
No	SW1	SW2	Sens. [mV/uW]		BW [MHz]		Sens. [mV/uW]		BW [MHz]		Sens. [mV/uW]		BW [MHz]	
			405nm	650nm	min.	typ.	405nm	650nm	min.	Typ.	405nm	650nm	min.	typ.
1	L	M	0.23	0.45	80	100	0.56	1.125	60	80	0.15	0.3	110	120
2	L	M	0.45	0.9	80	100	1.125	2.25	60	80	0.3	0.6	110	120
4	M	L	0.9	1.8	80	100	2.25	4.5	60	80	0.6	1.2	110	120
8	M	M	1.8	3.6	80	100	4.5	9	60	80	1.2	2.4	110	120
16	M	H	3.6	7.2	80	100	9	18	60	80	2.4	4.8	110	120
32	H	L	7.2	14.4	80	100	18	36	45	60	4.8	9.6	90	110
64	H	M	14.4	28.8	65	80	36	72	30	50	9.6	19.2	70	90
128	H	H	28.8	57.6	45	55	72	144	20	35	19.2	38.4	45	55

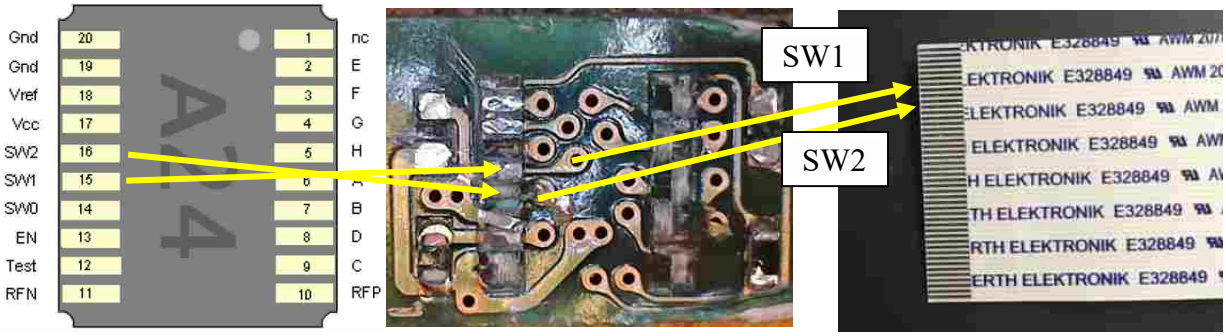

Figure 3-6: Circuit board behind PHR focusing photodiode. These traces were used along with the photodiode datasheet (Melexis MLX75012) to determine which pins on the circuit board corresponded to the photodiode controls.

3.3 Heating and Modulation Verification of Infrared Laser

To modulate the infrared laser, it was necessary to send it a sinusoidal voltage signal and analyze the laser output via photodiode to verify the sinusoidal shape. Multiple waveform generators were assessed to modulate the infrared laser. The least expensive waveform generator, an XR2206, did not output a steady frequency, and it was also difficult to tune the voltage output to get a smooth sine wave. If not tuned correctly, it would cut off the top or bottom of the wave. This chopped signal was examined with an oscilloscope's FFT analysis function to determine whether the dominant frequency would be prominent enough for the lock-in amplifier to use as the reference signal. The FFT showed a peak at the frequency, but it was not a steady output.

Additionally, this waveform generator could not offset the signal, which was necessary for some of the heating IR lasers that were used. The waveform generator built into the lock-in amplifier was also tested as the driver for the heating laser. This generated a very stable frequency, but was incapable of setting a DC offset. To correctly modulate the heating laser for data collection, an Agilent 33220A waveform generator was used. This device was capable of more detailed waveform customization and also of adding an offset to the signal. The ideal waveform was found to be a sine wave modulated between 2V and 3.3V, while it was capable of running at up to 5V, over 3.3V cut off the peak in the photodiode output. The ideal modulation voltage range was verified by directing it into a photodiode and finding the waveform amplitude and offset that did not cut off the signal at either the high or low end. The voltage range can be selected on the waveform generator where the tunable parameters of the waveform were frequency, high-end voltage, and low-end voltage. It would then produce a sine wave with the chosen frequency and modulated between the high and low voltages selected on the front numeric input pad.

To verify the heating capabilities of the infrared lasers they were focused onto a thermocouple to examine if there was a measurable temperature rise. With the infrared laser built into the PHR there was no temperature rise, leading to the purchase of an external laser diode. For the euro sample, an 85mW 780nm diode (L785P090) controlled by a ThorLabs LDC205C Laser Diode Controller was used. 100mm and 300mm plano-convex lenses were placed over the 780nm diode simultaneously to focus the beam onto the sample surface. This laser was replaced by a $32 150mW 780nm laser with built in current control from Aixiz lasers. This laser was much less expensive, smaller, and was verified with a thermocouple to produce a measurable temperature increase. It was easier to place in the set up and adjust the beam direction. The ThorLabs laser was more expensive, but the diode was interchangeable with other ones, making it useful for testing other diodes with different wavelengths or powers.

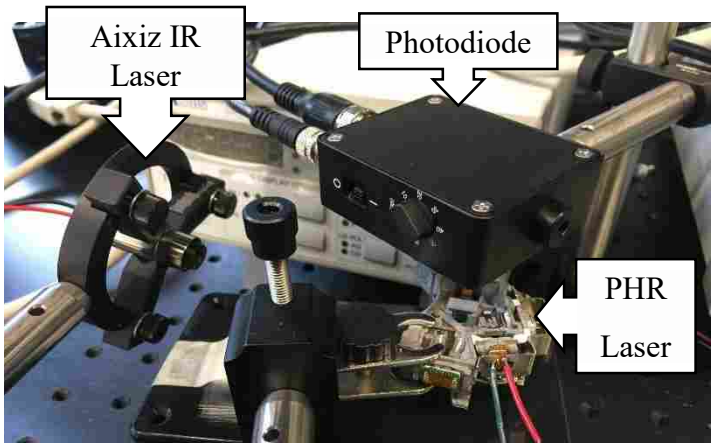

Figure 3-8: Experimental set up. PHR assembly with the amplified photodiode suspended above it. The IR laser is angled onto the sample from the side, but in the final version is held in a custom assembly.

A custom unit was designed to house the lasers, optics, and electronics in a convenient unit. The part shown below in Figure 3-7 was designed to hold the heating laser in line with the PHR's built in optical entry point for the infrared laser. When lined up correctly, the IR laser was directed into the side of the PHR, through though optics, and out the lens above the sample, coming out at the same point as the blue laser.

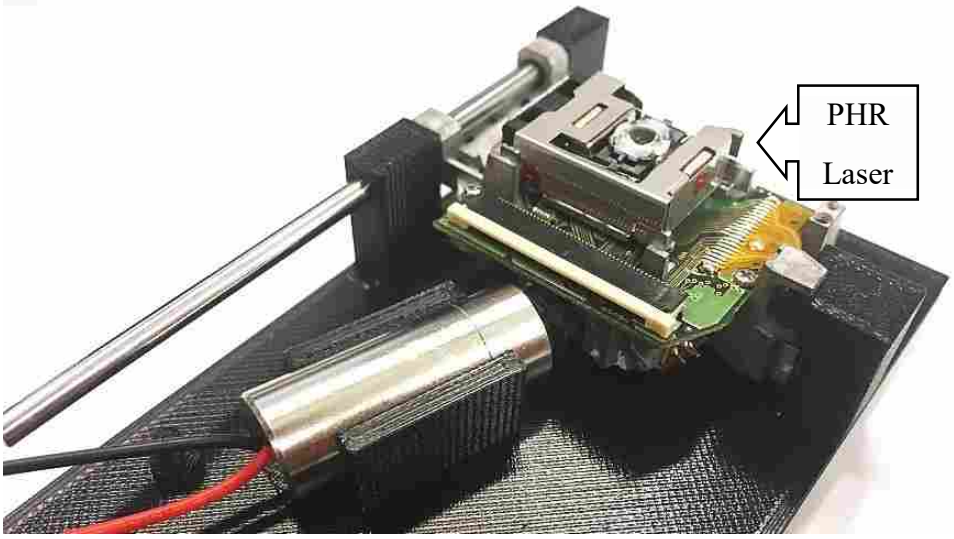

Figure 3-7: Custom designed piece to hold PHR laser assembly and the IR laser in line with the optics

3.4 Focusing

To achieve a small fluorescent spot size within the heating region on a variety of surfaces a consistent focusing system is necessary. Focusing the blue laser also maximizes the power absorbed by the fluorescent dye and increases its emission. A circuit developed by Diyouware [36] controls the three laser diodes, moves the lens up and down, and outputs the photodiode signal necessary for focusing. The movement of the lens is actuated by a voice coil actuator, where motion is driven by a magnetic field and wound coil that produces a force when current runs through it. This type of actuator allows for a very compact motion system with fine vertical resolution for focusing the lasers. To focus the laser, we needed to develop a focusing code that followed the algorithm Diyouware generated in their program. Diyouware developed a graphical interface and program that could run focusing code, but for this project the Arduino code also needed to control the motors. The first step in the focusing process is slowly moving the PHR lens up and down, while recording the highest and lowest readings from the internal focusing photodiode. The position of the lens is controlled by changing the pre-scaler on certain PWM capable pins identified through the Arduino Mega datasheet. The duty cycle of the PWM signal is sent through a MOSFET driver to a voice coil motor. The photodiode built into the PHR laser assembly has four quadrants, shown in Figure 3-9, that collect reflected light; A, B, C, and D.

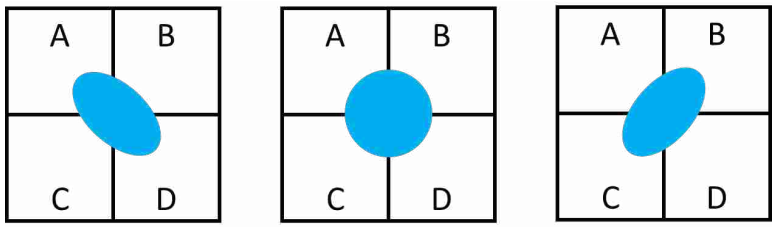

Figure 3-9: Focusing states bases on the light reflected back onto the focusing diode. The left and right images result when the lens is too close or too far. The center is when the laser is in focus.

When (A+C) – (B+D) equals zero the laser is focused. As the lens moves up and down, a voltage spike, called and S-curve, is generated by the photodiode. The PHR was focused using

both the blue and infrared laser to determine which was able to focus quicker and more consistently due to a more detectable signal. The signal that is being detected is called the S-curve. The S-curve is a voltage change that drops above and below the steady state signal value, and represents the region where the lens passes through the point of focus. Figure 3-11 shows that the amplitude of the S-curve generated by the internal focusing photodiode is much bigger when using the blue laser to focus. An Arduino Mega moves the lens up and down through the control circuitry (via code presented in Appendix D), reads in the focusing signal, analyzes it and stops the lens at the focus point. The amplitude of the S-curve is calculated as the difference between high and low amplitude values. An acceptable range of focus position is calculated as a region around the baseline signal from the focusing circuit. In Figure 3-10 the focus range is shown as the amplitude of the S-curve divided by 16. The lens moves up and down repeatedly until the program registers that the signal is in the a/16 region, and the lens is held at that point to collect data. Once the blue light is in focus, the IR laser heats the sample and the fluorescent emission is collected by the external photodiode. Because the blue laser is used for focusing, there is an unfocused IR beam that is larger than the blue spot, potentially allowing for the 1D heat transfer assumption, if only the *z* direction is analyzed.

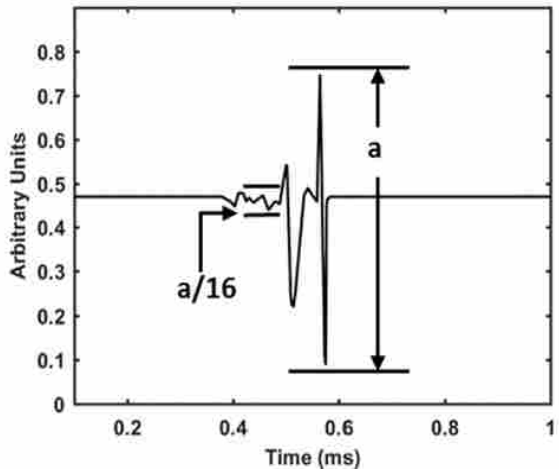

Figure 3-10: Diagram of the S-curve generated by the internal focusing diode. The amplitude and focus region are denoted by a and a/16 respectively.

3.5 Fluorescent Detection

With the lasers functioning and focused, it is then necessary to capture the emitted fluorescence for analysis. To verify the emission wavelength and intensity, the emission from euro the coin shown in Figure 3-12. The absolute intensity varies at each location due to varying concentration of the dye across the sample. The first set up for collecting the emission was a fiber optic cable positioned above a hole in the metal cover at the top of the laser assembly. Using a spectrometer, the fiber was incrementally moved above the opening to locate the position of highest transmitted fluorescent emission. Eventually, the fluorescent light emitted from the sample was collected by removing the metal cover from the top of the PHR-803t to increase the amount of fluorescence received by the photodetector and mounting an amplified Si photodiode (Thorlabs PDA36A) directly above the laser assembly to collect as much light as possible. The photodiode was used instead of the spectrometer to collect data because it is easier to collect pass the photodiode output into the lock-in amplifier for comparison. With the spectrometer it would be very difficult if not impossible to output a signal readable by the lock-in. The unfiltered light entering the photodiode detector contains ambient light, 785nm IR light from the heating laser, 405 nm blue light from the probe laser, and fluorescent light.

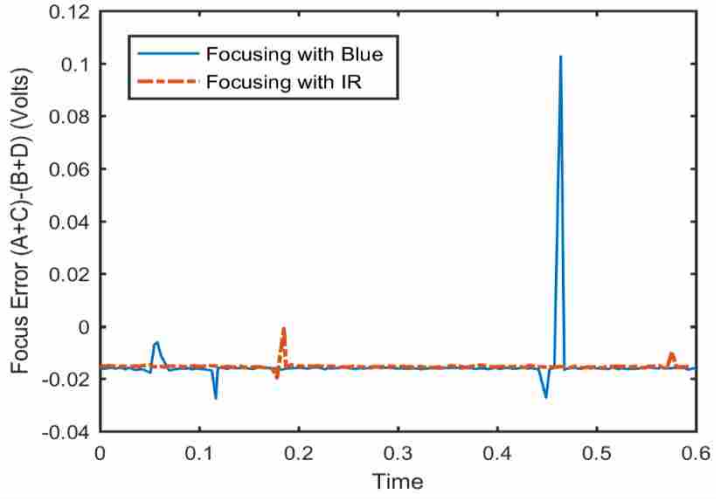

Figure 3-11: Amplitude of the S-curve when focusing with the PHR's blue vs. focusing with the PHR's infrared laser

Approximately 0.6mL of a 1.075g/mL of the fluorescent Rhodamine B (RhB) dye was deposited via dropper onto the Nordic Gold (89 Cu-5 Al-1 Sn) euro coin sample, left to dry, and excited by the probe laser to induce fluorescent emission. The upper right area of the coin has a different color due to a higher concentration of dye, with a dark ring around the area formed when the drops of dye dried as seen in Figure 3-12. The fluorescence from the coin was analyzed by a StellarNet Green-Wave spectrometer and shown in Figure 3-13 at four locations on the sample Figure 3-13 shows the unfiltered light counts at the excitation and emission wavelengths when the RhB was excited by the 405 nm laser, with the RhB's peak emission near 610 nm when the. To isolate the temperature dependent fluorescent emission, multiple optical filters were placed over the photodiode. A 550nm longpass filter removed the blue light, and a 750nm shortpass filter removed the IR laser emission. The adjustable gain photodiode (70dB, Thorlabs model mentioned previously) amplified the light signal and output a time varying voltage signal proportional to the fluorescence to be compared to the reference signal by the lock-in amplifier.

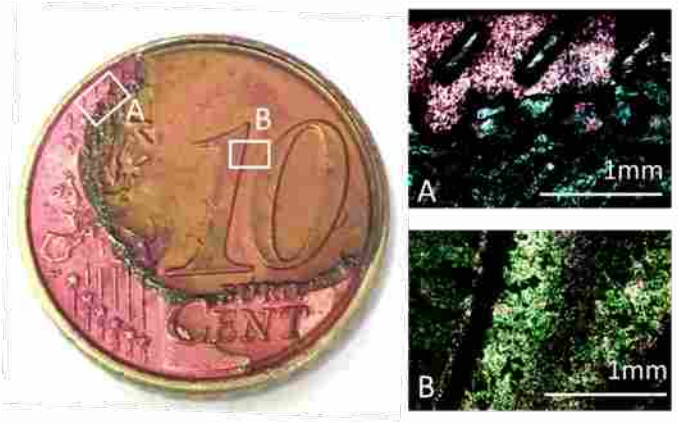

Figure 3-12: Image of coin with RhB deposited on surface. The color is different in certain areas due to the concentration of the dye regions. A and B show magnified images of the samples surface and how the distribution is uneven even at the mm scale, as well as the non-mirror like surface.

Fluorescent thermometry was chosen as the method of temperature sensing for multiple reasons. Because the PHR laser assembly already contains a 405nm blue laser, it works well for fluorescent methods. Because the blue laser can be used to induce fluorescence, it will work for this method where the sensor does not need to touch the sample's surface. Other methods for measuring temperature would include analyzing the other side of the sample for a temperature increase, thermocouple pads, or reflectance methods. These are more complicated to set up and require a more complicated preparation process.

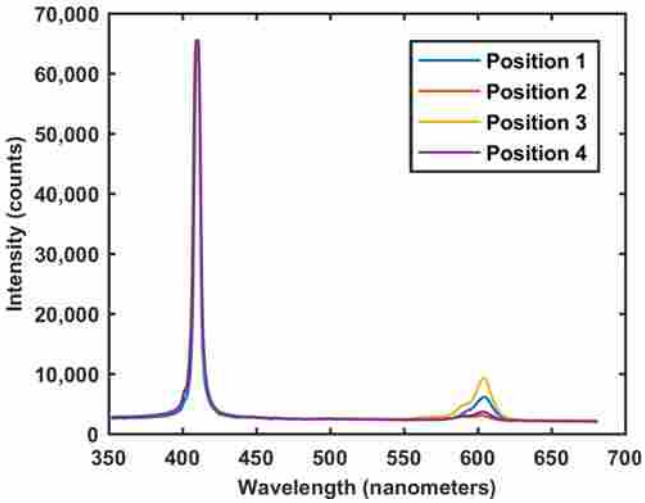

Figure 3-13: Graph of light intensity captured by a StellarNet Green-Wave spectrometer that measures between 350nm-1150nm. The peak at 405nm is the blue pump laser light, and the smaller peaks at 610nm are the fluorescent emission taken at four different locations on a sample.

3.6 Lock-in Detection

The SR830 lock-in amplifier received the noisy signal from the amplified photodiode and isolated the component at a frequency selected by the reference wave from the waveform generator. The signal was sent by BNC to both the laser driver for modulating the IR laser, and to the lock-in amplifier as the reference signal. The lock-in amplifier collected the fluorescent signal from the photodiode, compared it to the reference signal from the waveform generator, then output the phase delay between the two signals. The phase delay data (ϕ_{total}) was collected with MATLAB from

the lock-in amplifier connected to the computer via a GPIB-USB connector. To determine the phase delay (ϕ_{inst}) inherent to the electronics, the phase delay of the amplified photodiode illuminated solely by modulated IR light was also measured over the frequency range. This instrumentation phase delay was subtracted from the measured phase from the photodiode during the fluorescent measurements, and the resulting phase delay ($\phi_{thermal}$) of the temperature dependent fluorescent signal was fit to a frequency domain model of the heat diffusion equation to determine the thermal diffusivity.

3.7 Motors and Sample Movement

To move the sample beneath the PHR, while the PHR is held fixed, it is necessary to control motors with a repeatable movement distance for each step. The Xbox disc player assembly contains a motor to move the PHR laser assembly along the radius of the disc. This was that first motor we attempted to use to move the samples. This motor is shown below in Figure 3-14, and the data sheet is included in Appendix A. The motor was controlled via serial interface through an Arduino program. The goal of controlling the motors was to input a desired direction and have the motor move to that point. The program was set up to accept an input value of micrometers, then the motor was stepped the according number of rotations that theoretically resulted in a displacement of the entered distance. Via microscope and calibration slide, shown below in Figure 3-15, the distance of movement distance was verified and compared to the value that had been entered into the Arduino control program. This was done in Matlab by measuring the pixel distance moved and converting to micrometers based on the calibration ruler. The resulting distance verification showed that the motor was not consistent in its movement. This is shown below in Figure 3-16, where the actual location is shown to oscillate around the ideal value based on the

program input. Because of the imprecise control. A different motor was chosen to place in the overall product assembly and move the sample.

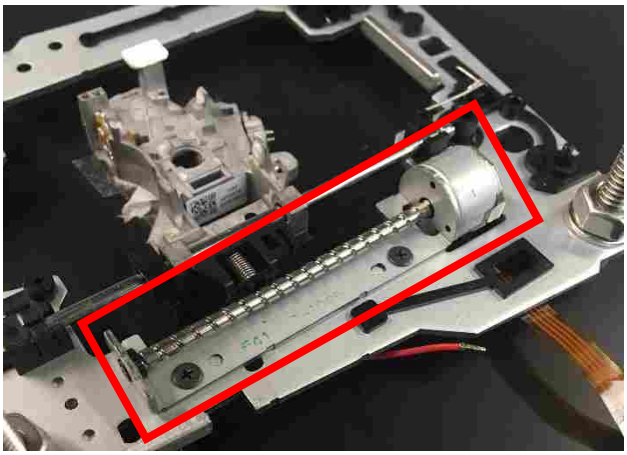

Figure 3-14: Motor included in the Xbox assembly for moving the PHR laser assembly over a disc

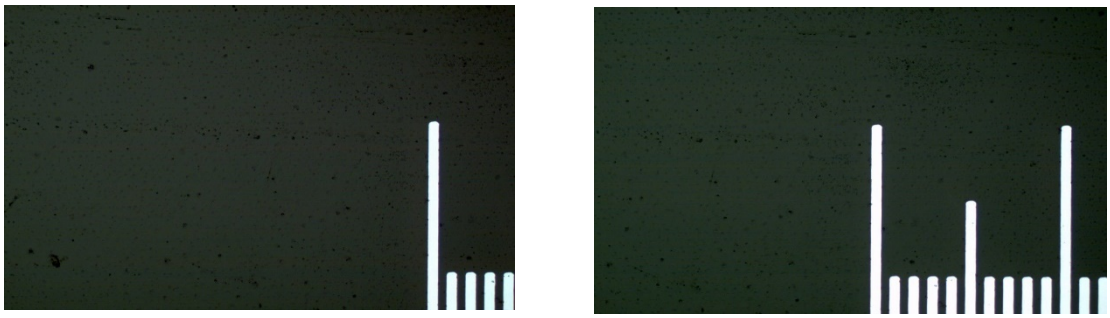

Figure 3-15: Microscope images of calibration slide attached to motor to verify movement distance

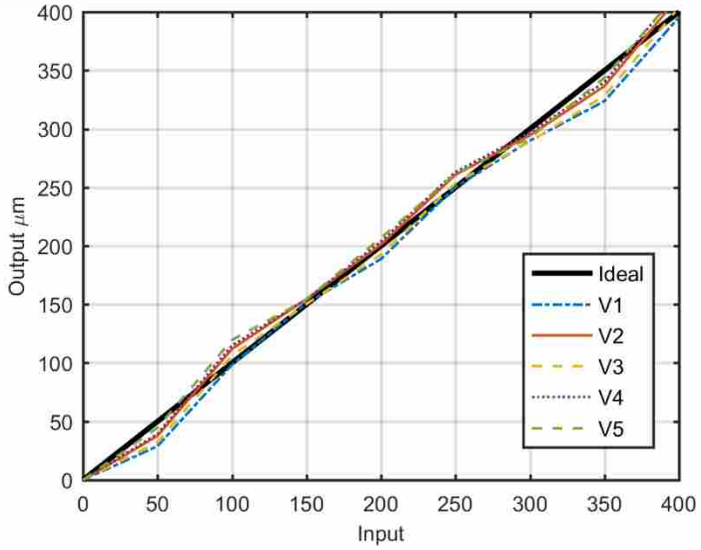

Figure 3-16: Actual vs. Ideal motor location based on program input and measured location

4 RESULTS AND DISCUSSION

This chapter presents the thermal property results gathered on two different samples using the FSTM and a heat transfer model from the literature. These samples include a 10 cent euro coin and a thin film of uranium dioxide deposited on silicon. These samples were chosen because of their rough surface for testing the capability of measuring minimally prepared samples, because of their homogeneous structure, and to determine if the FSTM could be used on nuclear materials. Each sample was analyzed to determine the thermal diffusivity and the methods unique to each sample are discussed in the following sections. The collected data sometimes predicted values that were outside of a physically possible range, or orders of magnitude off from the thermal diffusivity values for a metallic material. These criteria were used as judgement to determine whether the data would be used or not. The instrument phase delay was also affected by how the lasers were set up, meaning it needed to be measured before each test to produce the most consistent data. If not done correctly, the phase delay increased with frequency and the data needed to be retaken.

A heat transfer model from [39] was used to analyze the data. The model is a 3D Cartesian representation of the frequency domain temperature variations on the surface of an n-layered sample. The chosen model assumed no heat loss from the sample's surface, because the analysis in [39] found the effects of radiation and convection to be minimal in the frequency range of data collection. It also assumes that the substrate is semi-infinite as long as the laser heating spot is 10 times larger than the thermal diffusion length. With the collected phase delay data, a property for

the sample was guessed, and an optimization routine varied the thermal diffusivity until the error between the model and data points was minimized, with the output being the thermal diffusivity that generated the curve with the least error. Thermal waves and the model are discussed in detail in Appendix B.

The euro coin had experimental data collected by associates at Idaho National Labs or Utah State University to provide a comparison with properties measured by the FSTM. A theoretical models was also examined to calculate the effective thermal diffusivity of the euro based on material properties and the definition of thermal diffusivity ($\alpha = k/\rho c_p$), for comparison to experimentally determined values. The method for collecting data on the FSTM and analyzing it in MATLAB is discussed in Appendix E. The curve fitting process is discussed and the values & methods of determining thermal diffusivity are presented in a tabular format. The results show that the thermal diffusivity measurements were highly uncertain and require more in modeling and instrumentation work to improve on them.

4.1 Euro Coin Data Collection

The first test sample for the FSTM was a 10 cent euro coin. Data was collected using the external 90mW 780nm laser modulated between 80 Hz and 1 kHz, while the optical head's blue laser was used to induce fluorescence, and the optical head's built in photodiode was used to focus the blue laser on the sample. Above 1kHz, the data that was collected became too noisy and inconsistent to calculate reasonable properties. On metallic samples, the thermal diffusivity is relatively high and the phase delay will decrease slowly as frequency increases, as seen by the low magnitude of the highest frequency phase delay (roughly -3º) shown in Figure 4-1. While the decreasing trends in the total phase delay is apparent on the three samples, the trend in the net phase delay ($\phi_{thermal} = \phi_{total} - \phi_{inst}$) is less consistent. The fluorescent component of the

phase delay makes up a small part of the overall signal, so when subtracting them, uncertainty is larger relative to the net delay. At each location on the coin, and for each frequency, five seconds of data was collected five times. The five points at each frequency were analyzed to find the mean and standard deviation. Figure 4-2 presents thermal diffusivity measurements at these five spatially distributed data points on the euro coin. Each location in Figure 4-2 has a frequency vs. phase profile like that shown in Figure 4-1, which shows the different measured phases and best fit line to equation 12. The fitting algorithm was a Levenberg Marquardt non-linear fitting process that started with a preliminary thermal diffusivity input by the user. The starting value is used to generate a plot of phase delay vs. frequency using the model detailed in the previous chapter. The thermal diffusivity value is then varied until the error between the modeled curve and data points is minimized.

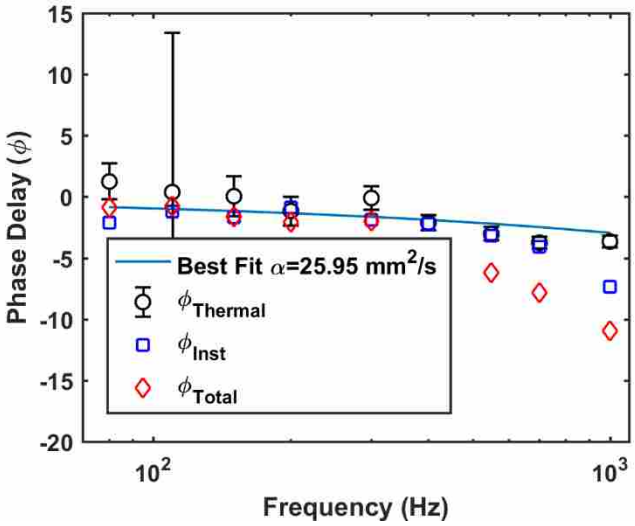

Figure 4-1: Curve fit results for euro coin

The average measured value of the euro coin by FSTM was α=21±5 mm^2/s, based on measurements at multiple locations and the standard deviation of the five data points shown in Figure 4-2. The goodness of fit was checked by calculating the square root of the sum of the residuals squared for a property fit 10% above and below the value found by the Levenberg

Marquardt process (i.e. 19 and 23 mm^2/s). The best fit line had a residual value of 3.61°, while the higher and lower properties resulted in 3.62° and 3.62° respectively, verifying the goodness of the initial fit. Thus, the fitting error was less significant than the standard deviation of multiple measurements and will be ignored in the uncertainty analysis.

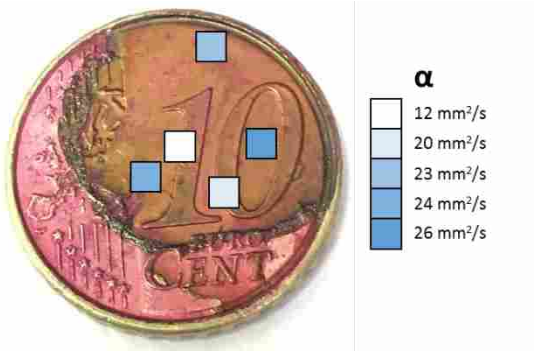

Figure 4-2: Image of sample with location of data points and resulting values overlaid.

The thermal diffusivity of the coin was then compared to other established methods, namely a thermal conductivity microscope (TCM, [24]) and laser flash. The TCM took several spatial scans at 1, 2, 5, and 10 kHz on a third euro sample that was highly polished and coated with approximately 35 nm of gold. The spatial scans involved in the TCM method involve a stationary pump laser that heats the sample and a probe laser that scans away from the heating spot as the phase delay between the input heating and temperature response is collected. This is shown in Figure 1-6, and the results of the fitting based on models in [24] are shown in Figure 4-3. In Figure 4-3 the spatial scans at different frequencies are shown with the collected data shown as points and the best fit results as a solid line. The resulting property was 19±3 mm^2/s, where the uncertainty represents the standard deviation of 15 measurements taken at different locations on the coin. Laser flash was performed on a separate euro coin sample after both faces were polished and coated with a thin layer of graphite. A Netzsch LFA 427 was used, resulting in α=30.4±0.1 mm^2/s. On an inhomogeneous sample, the comparison to LFA results would be irrelevant, since the FSTM measures spatially varying properties and the LFA measures bulk. However, since the euro is

homogeneous the thermal diffusivity results should be similar and are worth comparing. Finally the Wiedemann-Franz law ($k = LT\sigma_{elec}$) [40] was used to approximate the electronic contribution to the thermal conductivity, which is expected to dominate in a metal. Using a constant σ_{elec} from [41] and the Lorenz number (L) of $2.44 * 10^{-8}\ W\Omega K^{-2}$, thermal conductivity over a range of temperatures was determined. To compare the thermal diffusivity by FSTM, and TCM, to the Wiedemann-Franz model, the definition of thermal diffusivity ($\alpha = k/\rho c_p$) was used, where density (ρ) and specific heat (c_p) were predicted from the alloy composition of Nordic Gold, which is the name for the alloy used in euro coins. The results for the euro coin in Table 4-1 show that the FSTM method found properties in the range of the other well-established methods, but with higher uncertainty.

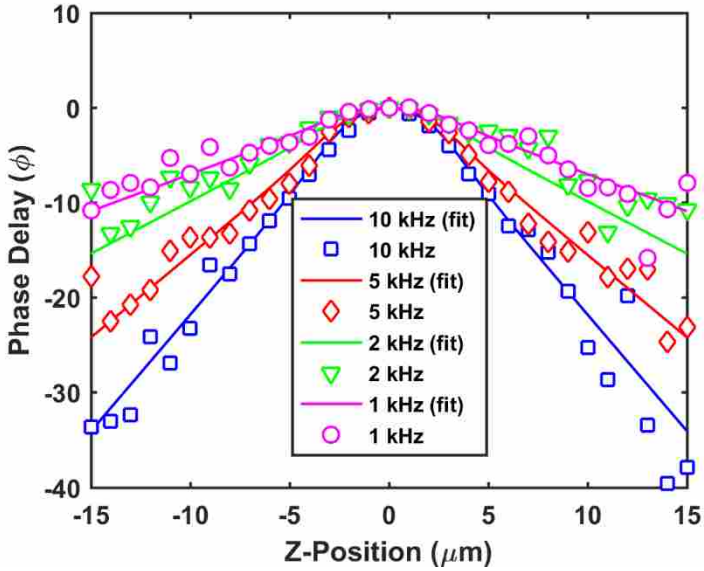

Figure 4-3: Curve fit on data collected with TCM on euro coin

4.2 UO_2 Data Collection

The second sample was a piece of silicon with a thin film of UO_2 deposited on the top surface. The sample is shown below in Figure 4-4. The RhB was deposited onto the surface in successive drops, letting the toluene dissolving agent evaporate between applications.

The data collected on the 500 nm UO_2 film sample by the FSTM resulted in an effective thermal diffusivity of the film/substrate of α_{eff}=13mm^2/s. Other measurements by the TCM on a UO_2 sample from the same wafer calculated the thermal diffusivity as 74.4 mm^2/s. One key difficulty with these measurements was the unknown thermal properties of the silicon substrate, and because the film was so thin and the substrate so conductive, slight changes in substrate properties had massive effects on the fitted value for the thermal diffusivity. This is a common issue with inverse problems, as they are ill-posed. Additionally, the signal to noise ratio of the film was lower than what was seen with the euro coin.

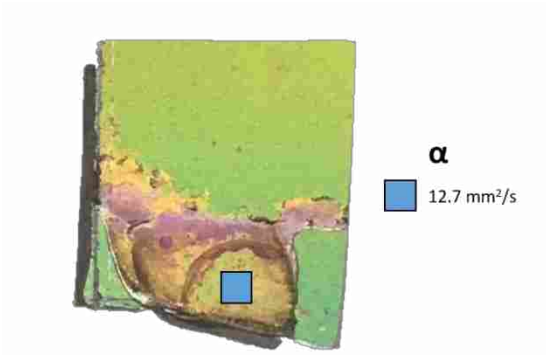

Figure 4-4: UO_2 sample with RhB deposited on the surface

All the thermal conductivity values collected from each method on each sample are presented in Table 4-1.

Table 4-1: Comparison of values calculated with various methods, all in units of mm^2/s.

	FSTM	*LFA*	*TCM*	*THEORETICAL*
EURO	**21±5**	30.4±0.1	19±3	26
UO_2	**13**[1]	-	74.4[2]	-

[1] film/substrate values

[2] film value based on *k = 60 W/m-K* for the Si substrate measured at INL

4.3 Error Analysis

There are a variety of potential sources of error in the FSTM that will be briefly assessed, along with an analysis of quantifiable comparisons of systematic and random error to investigate the validity and consistency of the data presented in the previous chapter.

4.3.1 Potential errors from device design

Potential sources of error in the data include loss of fluorescence intensity and lower signal to noise ratio as the light is emitted from the sample and as it travels through the optical head to the photodiode. As seen in Figure 3-1, the fluorescence from the sample leaves the surface of the coin, travels back through the lens, passes through a beam splitter and multiple optical filters, and is then detected by the amplified photodiode.

The distance from the sample to the photodiode collector, and components between them, result in loss of signal strength as a sizable portion of it is emitted to the surroundings, absorbed, or blocked by hardware. To minimize this effect, the photodiode is placed close against the top of the optical head where the fluorescent exits the assembly. The metal cover on the top of the optical head was removed to minimize the material between the amplified photodiode and fluorescence. The attenuated fluorescent signal results in error and variation between data collection sets. Other sources of error include difficulty in aligning the pump and probe laser spots and ensuring strong fluorescent emission from the fluorescent dye deposited on the sample. Aligning the IR and blue laser may also introduce error into the data as the current model uses concentric laser beams to represent the pump and probe laser spots. The external heating laser is aligned as best as possible with the blue laser on the sample, but if not aligned correctly, the fluorescence is not modulated at the center of the heating spot. This alignment is necessary for some of the assumptions in the model of the heating system. Fortunately, the blue laser spot is easy to see when aligning and it is possible

to place the blue laser in the center of the IR heating spot via visual inspection of a faint red dot emitted from the 780nm diode in addition to the invisible IR light. The red light was a higher wavelength than the fluorescence and was filtered out before reaching the photodiode.

4.3.2 Statistical error analysis

To assess the results and determine the validity of the FSTM's thermal diffusivity values, a t-test at the 5% confidence interval was done on the sets of data from the FSTM, LFA, and TCM for the euro. Even though the FSTM and LFA measure different property scales, the results worth comparing for the euro because it is homogeneous and should result in similar results. A t-test measures two sets of data to evaluate the null hypothesis that the difference in the means is zero. If the null hypothesis is not rejected, then the differences in the mean thermal diffusivity values can be attributed to randomness and not to systematic (or instrument related) errors. To compute the t value in a two sample t-test, the equation 15 is used to compare the difference in the mean to the difference in the magnitude of the normalized variance in each data set.

$$t = \frac{\overline{\alpha_1} - \overline{\alpha_2}}{\sqrt{\frac{s_{\alpha_1}^2}{n} + \frac{s_{\alpha_2}^2}{m}}} \tag{2}$$

The resulting t-values are compared to a t distribution value based on the percent probability that the null hypotheses can be rejected. If the calculated t value is less than the t distribution in Table 4.4 of [43], then the null hypotheses may not be rejected and the differences in the measurements from different devices can be attributed to randomness. Table 4-2 presents the t-test results for the euro coin between each of the three methods used to measure the thermal diffusivity. As seen in the t-test results, the measurements from the FSTM and the TCM are close enough in the mean thermal diffusivity that the difference can be attributed to random error. But

when comparing the FSTM to the LFA the error is more significant than randomness. However, the similarities in the FSTM and TCM measurements bodes well, as they are both microscopic measurements of α.

Table 4-2: T-test results for the euro. If the null hypothesis is not rejected, the results are close enough between the systems that the difference can be attributed to random error.

EURO	*t*	*Null Hypothesis*	*Result*
FSTM-LFA	3.9	Reject	Difference due to system error
FSTM-TCM	0.7	Not rejected	Difference within random error
LFA-TCM	11.3	Reject	Difference due to system error

Based on this statistical analysis, we can conclude that the measurements of the FSTM are statically comparable to those by TCM when using the same heat transfer model. However, there is a significant amount of uncertainty on the FSTM measurements (~25% from the standard deviation of measured values, with uncertainty to increase when considering modeling effects).

4.4 Cost Assessment

Because the development of the FSTM was partially focused on providing a cheap device, the cost of the different components must be considered and is presented in Appendix C. The vast majority of the cost is comprised of the lock-in amplifier. With the future development of a cheap, specialized lock-in, the goal of a more cost-effective thermal characterization microscope can more fully be realized. Among other methods researched, this FSTM method is least expensive. Difficulties with the PHR-803t include a weak infrared laser and the limit of only turning one laser on at a time with the built-in control circuitry. To overcome, this an aftermarket IR laser was

incorporated into the set up and the blue laser is controlled through the built-in circuitry. The optical head's infrared laser will then be replaced with a more powerful laser diode. The resulting total cost is shown in the Bill of Materials in the Appendix C.

5 CONCLUSION

The thermal diffusivity value found by the FSTM microscope fall between the measured values from the other experimental data (LFA, TCM) but are statistically uncertain, with only one result falling within random error instead of systematic or modeling error. These measurements were based on statistical t-tests. When compared to the LFA the difference is statistically outside random variation and indicates error within the FSTM system, even though it is a homogeneous sample with consistent properties throughout. But interestingly in the t-test comparison between the LFA and TCM (both well-established methods), the results were outside the range of random error as well, even though they were both measuring a homogeneous sample. Overall, the property measurements are highly uncertain and the device and indicate that the heat transfer model likely doesn't work and needs further refinement.

Comparing the physical functioning of the different methods, TCM requires polishing the sample down and coating it in a reflective metal. These requirements are not always feasible, because it is possible that the surface to study is rough and polishing may remove the structures of interest. For the method demonstrated in this thesis, surface preparation was limited to preparing the fluorescent dye solution, depositing an adequate amount onto the sample, and letting it evaporate. The FSTM method does not require access to both sides of the sample, as both lasers and detecting instrumentation are suspended above one side of it. The sample used to collect data was not polished, but the modeling may need further investigation to work with rough sample

surfaces. There is a need for refinement to achieve more certain results, especially in preparation for nuclear fuel analysis.

The objectives of the project included heating, scanning, collecting data, using the appropriate model for the system, and calculating properties on a known and unknown material sample. The device hardware and instrumentation performs as expected, but the accuracy of thermal measurements is not yet confirmed. The device was verified to heat samples adequately using an inexpensive infrared laser by shining it on a thermocouple for measuring a temperature change. The motor scanning is on the desired length scale, but the step size is not as repeatable as hoped. The device was also able to collect the necessary fluorescent data via photodiode after experimenting with the best way to capture as much fluorescence as possible with the PHR, which ended up being an open PHR assembly with the amplified photodiode suspended above it, placed against the optical filters. The heat transfer in the sample was modeled based on the work in the literature that represented a sample with a thin layer on it that absorbs modulated heating from a laser. The model parameters that represented the density and specific heat of the material were adjusted to match the samples analyzed in this project. The FSTM was used to collect data and calculate the properties of a known material (the euro), and a material of unknown properties, related to nuclear fuels (UO_2). The results for the euro was closer to other methods, but highly uncertain, and the UO_2 piece was much higher than the data collected by TCM. While some results were in between or near those from the other methods, the variation in most of them indicated necessary systematic changes to increase the consistency of the results.

5.1 Limitations and Future Work

The results largely indicate substantial error in the system and/or model. The results presented in the previous chapter were achieved after many attempts at collecting data that related

to properties on the right order of magnitude. It is not yet consistent enough for commercial use. Sometimes the changes between tests that resulted in unreasonable and reasonable results were unnoticeable, and it is difficult to articulate or quantify why some tests came out well and some did not. The phase delay data for the euro coin lined up well with the best fit curve from the model and the predicted curve was within the uncertainty of the data points.

The heat transfer model needs to be examined in depth to investigate the following:

- Incorporating surface roughness effects into the model, as measuring rough surfaces is an advantage of the FSTM.
- Finding properties of RhB and incorporating thin RhB layer into the model.
- Modeling contact resistance, like the interface between the RhB and the substrate.
- Additional investigation of no heat loss assumption
- Role of surface roughness on applicability of existing heat transfer models.

The following lists future work to refine the instrumentation:

- Examining alternates to the PHR-803t to see if there is a better way to capture fluorescent data. One option for this is using just an Aixiz 405nm blue laser instead of the PHR-803t and putting the photodiode closer to the sample surface so that the fluorescence is not blocked by hardware.
- Future work also includes refining the assembly that houses all the electronics and components together.
- Developing circuitry and integration of a cheaper lock-in amplifier and waveform generator.
- Testing the FSTM on more materials to refine the range of materials that will work well with modulated fluorescent methods.

- Investigating movement of the PHR-803t lens in other axes to potentially offset the laser spot for spatially offset measurements, Diyouware [36] mentions the lens pins can be used to do so.
- Designing and testing a Nema 17 powered lead screw motion system.
- Taking measurements with the TCM may also be performed for comparison with the results collected on a standard reference material.
- Finally, because of the variation between the various measurement methods, the systematic error of the FSTM needs to be determined based on round robin measurements of standard reference samples.

REFERENCES

[1] Lakowicz, J.R., *Principles of Fluorescence Spectroscopy*. 2006: Springer US.

[2] Banerjee, S. and T.R.G. Kutty, *Challenges in Nuclear Materials.* Science and Culture, 2013. **79**.

[3] Nakamura, J., et al., *Thermal Conductivity Change in High Burnup MOX Fuel Pellet.* Journal of Nuclear Science and Technology, 2009. **46**(9): p. 944-952.

[4] Zinkle, S.J., et al., *Accident Tolerant Fuels for LWRs: A Perspective.* Journal of Nuclear Materials, 2014. **448**(1-3).

[5] Tonks, M.R., et al., *Mechanistic materials modeling for nuclear fuel performance.* Annals of Nuclear Energy, 2017. **105**(Supplement C): p. 11-24.

[6] Cahill, D.G., *Thermal conductivity measurement from 30 to 750 K: the 3ω method.* Review of Scientific Instruments, 1990. **61**(2): p. 802-808.

[7] Parker, W.J., et al., *Flash Method of Determining Thermal Diffusivity, Heat Capacity, and Thermal Conductivity.* Journal of Applied Physics, 1961. **32**(9): p. 1679-1684.

[8] Cahill, D.G., *Analysis of heat flow in layered structures for time-domain thermoreflectance.* Review of Scientific Instruments, 2004. **75**(12): p. 5119-5122.

[9] White, J.T., et al., *Thermophysical properties of U3Si2 to 1773K.* Journal of Nuclear Materials, 2015. **464**: p. 275-280.

[10] Whittle, K., *Nuclear fuel, part 2: operational effects*, in *Nuclear Materials Science*. 2016, IOP Publishing. p. 4-1-4-18.

[11] Abad, B., D.A. Borca-Tasciuc, and M.S. Martin-Gonzalez, *Non-contact methods for thermal properties measurement.* Renewable and Sustainable Energy Reviews, 2017. **76**: p. 1348-1370.

[12] Jo, S., et al., *Development of an online nuclear materials thermo-physical property database (THERPRO).* Journal of the Korean Physical Society, 2011. **59**(23): p. 1107-1110.

[13] Zhang, Y., et al., *A noncontact thermal microprobe for local thermal conductivity measurement.* Review of Scientific Instruments, 2011. **82**(2): p. 024902.

[14] Zhang, Y., et al., *A microprobe technique for simultaneously measuring thermal conductivity and Seebeck coefficient of thin films.* Applied Physics Letters, 2010. **96**(6): p. 062107.

[15] Chirtoc, M., et al., *1ω, 2ω, 3ω Scanning Thermal Microscopy (SThM) and combinations with thermographic, radiometric, pyroelectric and thermoelastic techniques; Principles and applications.* Advanced Techniques and Applications on Scanning Probe Microscopy, 2008: p. 197-247.

[16] Takahashi, Y. and M. Murabayashi, *Measurement of Thermal Properties of Nuclear Materials by Laser Flash Method.* Journal of Nuclear Science and Technology, 1975. **12**(3): p. 133-144.

[17] Rosencwaig, A., et al., *Detection of thermal waves through optical reflectance.* Applied Physics Letters, 1985. **46**(11): p. 1013-1015.

[18] Cahill, D. and R. Pohl, *Thermal Conductivity of Amorphous Solids above the Plateau.* Physical review. B, Condensed matter, 1987. **35**(8): p. 4067-4073.

[19] Shrestha, K. and K. Gofryk, *Thermal conductivity of actinide materials measured using the 3 ω method.* APS March Meeting, 2017.

[20] Malen, J.A., et al., *Optical Measurement of Thermal Conductivity Using Fiber Aligned Frequency Domain Thermoreflectance.* Journal of Heat Transfer, 2011. **133**(8): p. 081601-081601-7.

[21] Schmidt, A.J., R. Cheaito, and M. Chiesa, *A frequency-domain thermoreflectance method for the characterization of thermal properties.* Review of Scientific Instruments, 2009. **80**(9): p. 094901.

[22] Hua, Z., et al., *Spatially localized measurement of thermal conductivity using a hybrid photothermal technique.* Journal of Applied Physics, 2012. **111**(10): p. 103505.

[23] Labratories, I.N., *Laboratory Directed Research and Development 2017 Annual Summary Report.* 2017.

[24] Hurley, D.H., et al., *Local measurement of thermal conductivity and diffusivity.* Review of Scientific Instruments, 2015. **86**(12).

[25] Dilhaire, S., et al., *Heterodyne picosecond thermoreflectance applied to nanoscale thermal metrology.* Journal of Applied Physics, 2011. **110**(11): p. 114314.

[26] Liu, X.F., et al., *Thermal conductivity measurement of individual CdS nanowires using microphotoluminescence spectroscopy.* Journal of Applied Physics, 2010. **108**(5): p. 054310.

[27] Munro, T., et al., *Thermophysical properties of thin fibers via photothermal quantum dot fluorescence spectral shape-based thermometry.* International Journal of Heat and Mass Transfer, 2017. **112**: p. 1090-1097.

[28] Kasha, M., *Characterization of electronic transitions in complex molecules.* Discussions of the Faraday Society, 1950. **9**(0): p. 14-19.

[29] Reshma, V.G. and P.V. Mohanan, *Quantum dots: Applications and safety consequences.* Journal of Luminescence, 2018. **205**.

[30] Resch-Genger, U., et al., *Quantum dots versus organic dyes as fluorescent labels.* Nat Meth, 2008. **5**(9): p. 763-775.

[31] Munro, T., et al., *CdSe/ZnS quantum dot fluorescence spectra shape-based thermometry via neural network reconstruction.* Journal of Applied Physics, 2016. **119**(21): p. 214903.

[32] Glawdel, T., et al., *Photobleaching absorbed Rhodamine B to improve temperature measurements in PDMS microchannels.* Lab on a Chip, 2009. **9**(1): p. 171-174.

[33] Maruyama, H., R. Kariya, and F. Arai, *Evaluation of thermal conductivity of single carbon nanotubes in air and liquid using a fluorescence temperature sensor.* Applied Physics Letters, 2013. **103**(16): p. 161905.

[34] Moeken, H.H.P. and W.A.H. Van Neste, *Absorptiometric determination of microgram amounts of uranium with Rhodamine B.* Analytica Chimica Acta, 1967. **37**: p. 480-483.

[35] Lietzke, A.F., *Simplified Analysis of Nuclear Fuel Pin Swelling*, in *NASA-TN-D-5609*. 1970, NASA: Cleveland, Ohio.

[36] Victor. *Diyouware TwinTeeth: The PCB mini-factory*. 2013 [cited 2017; Available from: http://www.diyouware.com/.

[37] Walker, G.W., et al., *Quantum-dot optical temperature probes.* Applied Physics Letters, 2003. **83**(17): p. 3555-3557.

[38] Liu, L., et al., *Temperature-sensitive photoluminescent CdSe-ZnS polymer composite film for lock-in photothermal characterization.* Journal of Applied Physics, 2016. **119**(22): p. 224902.

[39] Hua, Z., *Hybrid Photothermal Technique for Microscale Thermal Conductivity Measurement*, in *Mechanical and Aerospace Engineering*. 2013, Utah State University.

[40] Kim, H.-S., et al., *Characterization of Lorenz number with Seebeck coefficient measurement.* APL Materials, 2015. **3**(4): p. 041506.

[41] Kolyshkin, A., et al. *Determination of electrical conductivity of metal plates using planar spiral coils*. in *Proceedings of the 13th WSEAS international conference on Systems*. 2009.

[42] *Cupronickel Properties*. Available from: http://www.matweb.com/search/DataSheet.aspx?MatGUID=4fb6ab47b8784e868bc270d230da8109&ckck=1.

[43] Richard S. Figliola , D.E.B., *Theory and Design for Mechanical Measurements.* 2015.

[44] Almond, D.P. and P.M. Patel, *Photothermal Sciences and Techniques*. Physics and its Applications, ed. E.R. Dobbs and S.B. Palmer. Vol. 10. 1996: Chapman & Hall.

[45] Pilla, V., et al., *Photothermal Spectroscopic Characterization in CdSe/ZnS and CdSe/CdS Quantum Dots: A Review and New Applications*, in *Quantum Dots: A Variety of New Applications*, A. Al-Ahmadi, Editor. 2012.

APPENDIX

Appendix A: Motor Datasheet used by HD DVD player and PHR Control Circuit Diagram

NMB-MAT

Minebea-Matsushita Motor Corporation

eMINEBEA.COM

PL15S-020

PM Motor
PL Type

Applications

Head Drive for Floppy Disk Drive
Pick Up Drive for CD
Pick Up Drive for DVD

Reference Characteristics

Motor Size	PL15S-020
Number of Steps per Rotation	20
Drive Method	2-2 PHASE
Drive Circuit	BIPOLAR CONST. VOLT.
Drive Voltage	5[V]
Coil Resistance/Phase	10[Ω]
Magnet Material	Nd-Fe-B bonded magnet (MS70)
Holding Torque	30[X10⁻¹ N.m]
Maximum PULL-IN Frequency	1450[PPS]

Typical Torque Characteristics

Driver Frequency	400[PPS]	1400[PPS]
PULL-OUT Torque	25[X10⁻⁴ N.m]	13[X10⁻¹ N.m]

Switching Sequence
(Viewed from Lead Screw Side)

STEP	A1	A2	B1	B3
1	−	+	+	−
2	−	+	−	+
3	+	−	−	+
4	+	−	+	−

CW ▼ ▲ M3.5

Torque Characteristics

PL LEAD SCREW TYPE(at 5[V], 10[Ω])

These torque values are reference only.
Heat radiation conditions and temperature rise effect by duty are different on each equipment, therefore please select motors after considering the heat conditions in the actual equipment.

Lead Screw Spec

OUTSIDE DIA.	φ3
MINOR DIA.	φ2
PITCH DIA.	φ2.4
PITCH	3.0
LEAD ANGLE	2°41' 45"
LEAD DIRECTION	RIGHT-HAND SINGLE THREAD
SIMPLE PITCH ERROR	0.020
CUMULATIVE PITCH ERROR	0.030

Dimensions

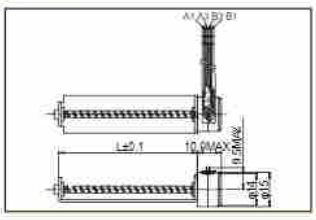

Detail of Screw

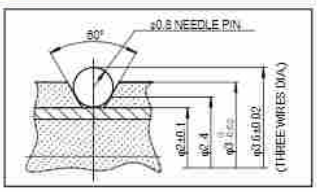

Performance values shown on this website are representative. Motor design and specifications are subject to change without notice.

Copyright 2001, Minebea Co., Ltd.

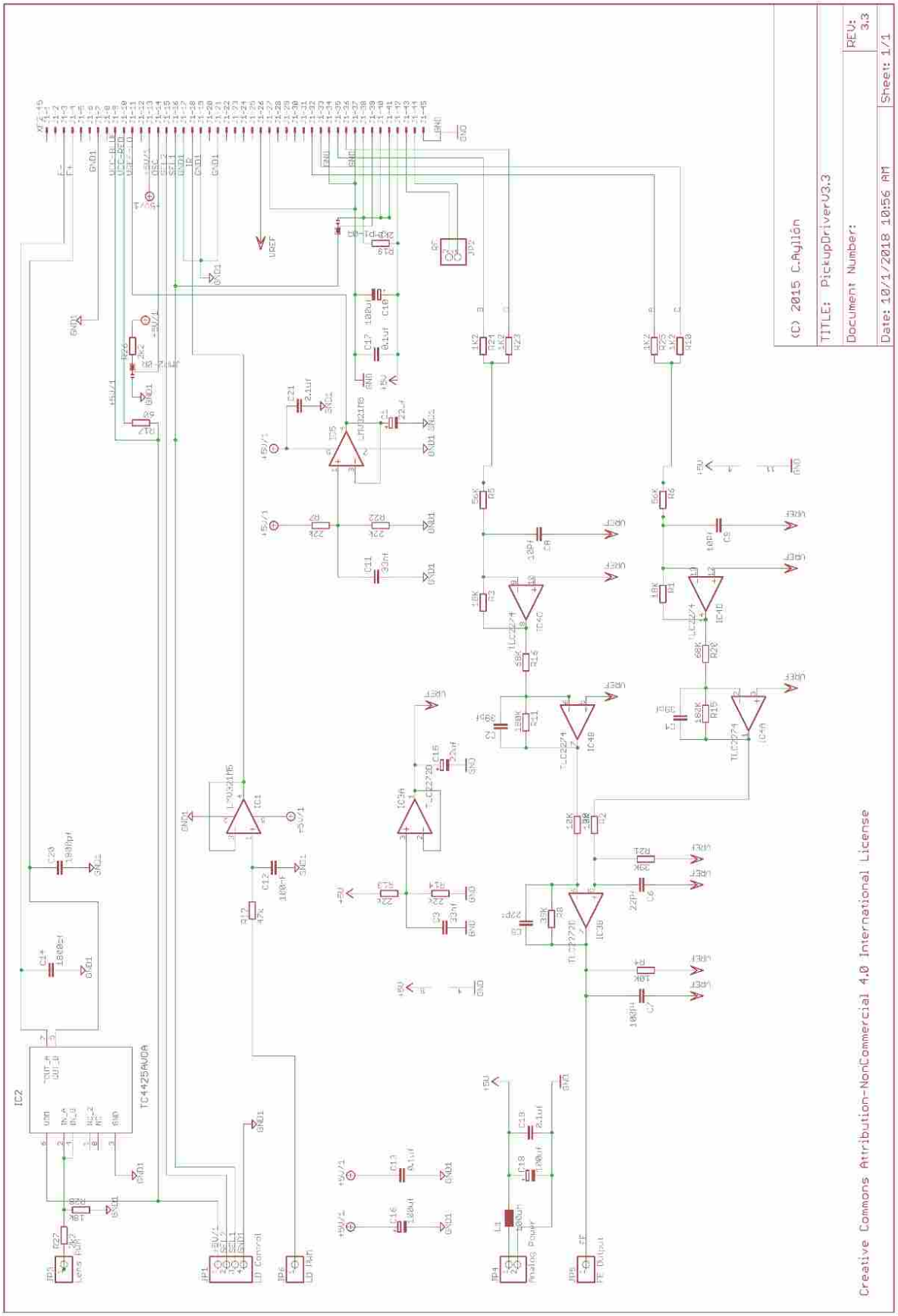
(C) 2015 C.Aylión
TITLE: PickupDriverV3.3
Document Number:
REV: 3.3
Date: 10/1/2018 10:56 AM
Sheet: 1/1
Creative Commons Attribution-NonCommercial 4.0 International License
TC4425AVOA
TLC2274
TL072IP
LM321M5
Lens Motor
LD Control
LD Mon
Analog Power
FE Output

Appendix B: Modeling

This section describes some fundamentals of periodic heat transfer analysis and the model that was used in the data analysis for this project. Periodic heating and mathematical analysis in the frequency domain has been used in many property characterization techniques, like those discussed in section 1.2.2, and simplifies the data collection involved. It is not necessary to measure the absolute temperature value and its transient change, but only the variation from steady state temperature. Therefore, the temperature of the sample or temperature fluorescence relation does not need to be calibrated. The model discussed in this chapter discusses the heat transfer analysis in the frequency domain for a laser heated sample in 3 dimensions and the capability of including different material layers and thicknesses within the sample.

Introduction to Periodic Heat Absorption and Transfer

As an introduction to periodic heating analysis, often characterized as thermal waves, we will first look at an isotropic homogeneous semi-infinite medium [44] that is periodically heated by a modulated laser.

In a 1D model the laser is treated as a boundary condition with the representation of

$$\frac{\partial^2 T}{\partial x^2} - \frac{1}{\alpha}\frac{\partial T}{\partial t} = 0 \tag{1}$$

$$-k\frac{\partial T}{\partial x}|_{x=0} = \frac{Q_o}{2}[1 + \cos(\omega t)] \tag{2a}$$

$$\frac{\partial T}{\partial x}|_{x\to\infty} = 0 \tag{2b}$$

$$T(x, 0) = T_i \tag{2c}$$

with $Q_o/2$ shown in equation 2a representing the laser power and DC offset when distributed to the first term in brackets, and ω the frequency of modulation. The transient heat equation in one direction will be used to solve for the temperature profile in this scenario. The boundary condition

will equate the conduction into the material to the periodic thermal energy from the laser at the surface.

$$-k\frac{\partial T}{\partial x} = \frac{Q_o}{2}[1+\cos(\omega t)] = \mathrm{Re}\left\{\frac{Q_o}{2}[1+\exp(j\omega t)]\right\} \tag{3}$$

where k represents the thermal conductivity of the material. The real part of the heating can be broken down into steady and transient terms, $\frac{Q_o}{2}$ and $\frac{Q_o}{2}\exp(j\omega t)$ respectively, when $\frac{Q_o}{2}$ is distributed through the expression. Only the transient part will be analyzed in the following solution. To solve the transient 1-D heat equation we will assume the periodic component solution is of this form:

$$T(x,t) = Re\left(\hat{T}(x)exp(\omega t)\right) \tag{4}$$

The quasi-steady solution to equation 1 becomes

$$T(x) = A\exp(-\sigma x) + B\exp(\sigma x) \tag{5}$$

$$\sigma = (1+j)\left(\frac{\omega}{w\alpha}\right)^{\frac{1}{2}} \tag{6}$$

where A and B are arbitrary constants and σ is defined in equation 6. The sample in the case of equation 2 is represented as a semi-infinite media. Assuming that $T(x)$ is finite as x goes to infinity, B is zero. The boundary condition in equation 2a-c represents the heat from the laser being equal to the conduction into the material at the surface and can be used to solve for the constant A in equation 5. Solving the equation out it results in

$$T(x,t) = \frac{Q_o}{2\sqrt{\rho ck\omega}}\exp\left(-\frac{x}{\mu}\right)\exp\left[j\left(\omega t - \frac{x}{\mu} - \frac{\pi}{4}\right)\right] \tag{7}$$

$$\mu = \sqrt{\frac{2\alpha}{\omega}} \tag{8}$$

where ρ, c_p, and k represent density, specific heat, and thermal conductivity of the material and μ is the thermal diffusion length of the periodic wave. The thermal diffusion length represents how far into the material the temperature change penetrates, characterizes the thermal wave, and is a function of the thermal diffusivity of the sample and frequency of the heating laser. This simple model will not work to calculate the phase delay of thermal waves, because with our method of temperature sensing, we can only measure the temperature at the surface of the material when $x = 0$. In this is the case, the terms with x disappear and the phase delay at the surface is a constant $\pi/4$. Additionally, this model does not work because of its 1D nature, the fact that it only accounts for a single material layer, and that the spatial distribution of the laser beam is not considered. In the experiments of the current work, the sample has a very thin layer of the fluorescent dye on the surface. Other works indicate that the quantum dot particles do not contribute significantly to the thermal diffusivity, and the RhB dye particles are assumed similar enough that it also applies [45].

Heat Diffusion Model

To relate the temperature dependent fluorescent intensity to the thermal diffusivity of the sample, it is necessary to solve the inverse problem applied to the heat diffusion equation and account for the heating depth in the sample and layered dye to find a property dependent phase delay. In [22, 39], a 3D model is developed that uses a heat generation expression in the heat diffusion equation to represent the absorption of the IR laser. This model was used for frequency domain experiments and can analyze the data taken with the FSTM. The model was developed to account for layered samples, and it can represent the fluorescent dye layered on the surface of the sample or it can be considered as two layers with similar properties. The single layer form was

used in this experiment based on the assumption that all of the infrared heating passed through the fluorescent layer and was absorbed by the sample. This was assumed because the Rhodamine was deposited as a mixture with toluene and then the toluene evaporated off of the sample, leaving only the small RhB particles. This model was developed in 3D to account for a spatial separation of the pump and probe laser if necessary. This may be possible in future iterations of the device, where the IR laser spot can be moved to produce a spatial offset between the laser spots. The governing equation of the 3D model is as follows, and the physical representation of it is shown in Figure A-1,

$$k_{fij}T_{f,ij} - \rho_f c_f \dot{T}_f = Q_f \tag{9}$$

$$k_{sij}T_{s,ij} - \rho_s c_s \dot{T}_s = Q_s \tag{10}$$

with the following terms for the Gaussian distributed heat sources,

$$Q_f = \frac{P\alpha_f(1-R_f)}{\pi a_1 a_2}\exp\left(-\frac{x_1^2}{a_1^2}-\frac{x_2^2}{a_2^2}-\alpha_f x_3\right)\left(\frac{1}{2}+\frac{1}{4}(\exp(i\omega t)+\exp(-i\omega t))\right) \tag{11}$$

where P is the power of the pump laser and a_1 and a_2 are the major and minor axes of the heating laser spot, and R is the reflectivity on the surface of layers. The subscript f represents the film, and s represents the substrate, with h representing the film thickness. This model can also consider anisotropic thermal conductivity, with the directions represented by subscripts i and j, but was considered isotropic for the Nordic Gold coin. The surface temperature of the sample is derived in Fourier space as $\widehat{T_o}(\xi_1,\xi_2)$ with ξ_1 and ξ_1 and ξ_2 representing the integral variables. With the necessary boundary conditions, the inverse Fourier transform is performed numerically on equation 11.

$$T_o = \frac{1}{2\pi}\iint_{-\infty}^{\infty}\widehat{T_o}(\xi_1,\xi_2)\exp[i(\xi_1 x_1+\xi_2 x_2)]\,d\xi_1\,d\xi_2 \tag{12}$$

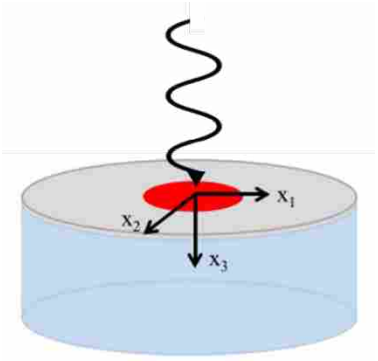

Figure A-1: Set up of system to be analyzed. The heating first hits the top layer of RhB particles and is transmitted to the substrate. The model can account for two layers denoted by f for film and s for substrate

In transform space, the solution is

$$\widehat{T_f} = A\exp(-\eta_f x_3) + B\exp(\eta_f x_3) + E\exp(-\alpha_f x_3) \tag{13}$$

$$\widehat{T_s} = C\exp(-\eta_s(x_3 - h)) + D\exp(\eta_s(x_3 - h)) + F\exp(-\alpha_s(x_3 - h)) \tag{14}$$

where coefficients A, B, C, D, and E and the η values are found with the mathematical methods shown in Appendix B of [39]. The model produces a curve like that shown in Figure A-2, where the properties of the euro coin were input as parameters and the film and substrate where assumed to be one material.

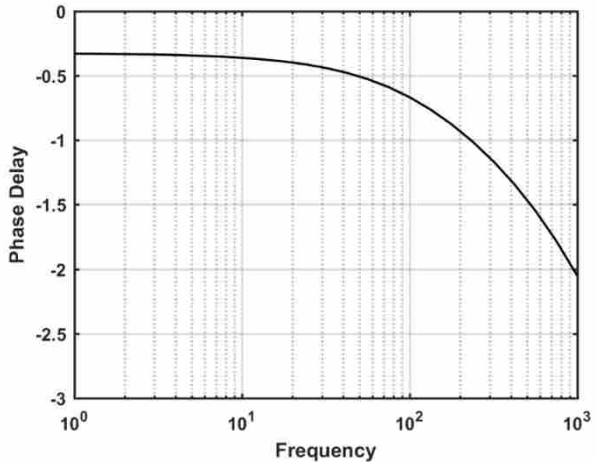

Figure A-2: Output of heat diffusion model using properties of Nordic gold, from 1 to 1000Hz

More detail is provided here on the model.

Governing equations:

$$k_{fij}T_{f,ij} - \rho_f c_f \dot{T}_f = Q_f \tag{15}$$

$$k_{sij}T_{s,ij} - \rho_s c_s \dot{T}_s = Q_s \tag{16}$$

Heat source terms:

$$Q_f = \frac{P\alpha_f(1-R_f)}{\pi a_1 a_2}\exp\left(-\frac{x_1^2}{a_1^2}-\frac{x_2^2}{a_2^2}-\alpha_f x_3\right)\left(\frac{1}{2}+\frac{1}{4}(\exp(i\omega t)+\exp(-i\omega t))\right) \tag{17}$$

$$Q_s = \frac{P\alpha_s(1-R_f)(1-R_s)\exp(-\alpha_f f h)}{\pi a_1 a_2}\exp\left(-\frac{x_1^2}{a_1^2}-\frac{x_2^2}{a_2^2}-\alpha_s(x_3-h)\right)\left(\frac{1}{2}+\frac{1}{4}(\exp(i\omega t)+\exp(-i\omega t))\right) \tag{18}$$

Boundary conditions:

$$-k_{f3i}\frac{\partial T_f}{\partial z}|_{z=0} = 0 \tag{19}$$

$$k_{f3i}\frac{\partial T_f}{\partial z}|_{z=h} = k_{s3i}\frac{\partial T_s}{\partial z}|_{z=h} \tag{20}$$

$$-R_{th}k_{s3i}\frac{\partial T_f}{\partial z}|_{z=h} = T_f - T_s \tag{21}$$

Normalization factors in 3 and 4 come from the following

$$\int Q_f dv = P(1-R_f) \tag{22}$$

$$\int Q_s dv = P(1-R_f)(1-R_s)\exp(-\alpha_f h) \tag{23}$$

which implies

$$Q_{f0} = \frac{P\alpha_f(1-R_f)}{\pi a_1 a_2} \tag{24}$$

$$Q_{s0} = \frac{P\alpha_s(1-R_f)(1-R_s)\exp(-\alpha_f h)}{\pi a_1 a_2} \tag{25}$$

To begin the solution a thermal wave solution is assumed below,

$$\breve{T}_j = \frac{1}{2}\left(T_j \exp(i\omega t) + T_j^* \exp(-i\omega t)\right), for\ j = s, f (\#26)$$

Then the thermal wave solution is substituted into the diffusion equation and $\exp(i\omega t)$ terms are collected

$$k_{fij}T_{f,ij} - i\omega\rho_f c_f T_f = \frac{P\alpha_f(1-R_f)}{\pi a_1 a_2}\exp\left(-\frac{x_1^2}{a_1^2} - \frac{x_2^2}{a_2^2} - \alpha_f x_3\right) \tag{27}$$

$$k_{sij}T_{s,ij} - i\omega\rho_s c_s T_s = \frac{P\alpha_s(1-R_s)(1-R_s)\exp(-\alpha_f h)}{\pi a_1 a_2}\exp\left(-\frac{x_1^2}{a_1^2} - \frac{x_2^2}{a_2^2} - \alpha_s(x_3 - h)\right) \tag{28}$$

Then a 2D Fourier Transform is applied to the equation above with respect to x_1 and x_2

$$-2\xi_1\xi_2 k_{f12}\hat{T}_f - 2i\xi_1 k_{f13}\hat{T}_{f,3} - 2i\xi_2 k_{f23}\hat{T}_{f,3} - \xi_1^2 k_{f11}\hat{T}_f - \xi_2^2 k_{f22}\hat{T}_f + k_{f33}\hat{T}_{f,33} - i\omega\rho_f c_f \hat{T}_f = \frac{P\alpha_f(1-R_f)}{2\pi}\exp\left(-\frac{\xi_1^2 a_1^2}{4} - \frac{\xi_2^2 a_2^2}{4} - \alpha_f x_3\right) \tag{29}$$

$$-2\xi_1\xi_2 k_{s12}\hat{T}_s - 2i\xi_1 k_{s13}\hat{T}_{f,3} - 2i\xi_2 k_{s23}\hat{T}_{s,3} - \xi_1^2 k_{f11}\hat{T}_s - \xi_2^2 k_{f22}\hat{T}_s + k_{f33}\hat{T}_{s,33} - i\omega\rho_s c_s \hat{T}_s = \frac{P\alpha_s(1-R_s)(1-R_s)\exp(-\alpha_f h)}{2\pi}\exp\left(-\frac{\xi_1^2 a_1^2}{4} - \frac{\xi_2^2 a_2^2}{4} - \alpha_s(x_3 - h)\right) \tag{30}$$

$$\hat{T}_f = A\exp(-\eta_f x_3) + B\exp(\eta_f x_3) + E\exp(-\alpha_f x_3) \tag{31}$$

$$\hat{T}_s = C\exp(-\eta_s(x_3 - h)) + D\exp(\eta_s(x_3 - h)) + F\exp(-\alpha_s(x_3 - h)) \tag{32}$$

The equation with coefficients E and F correspond to the particular solution for the film and substrate. To remain bounded, D must equal 0. The terms η_f and η_s are found by requiring that the homogeneous solutions satisfy the heat conduction equations:

$$k_{f33}\eta_f^2 + \left(2i\xi_1 k_{f13} + 2i\xi_2 k_{f23}\right)\eta_f - 2\xi_1\xi_2 k_{f12} - \xi_1^2 k_{f11} - \xi_2^2 k_{f22} - i\omega\rho_f c_f = 0 \tag{33}$$

$$k_{s33}\eta_s^2 + (2i\xi_1 k_{s13} + 2i\xi_2 k_{s23})\eta_s - 2\xi_1\xi_2 k_{s12} - \xi_1^2 k_{s11} - \xi_2^2 k_{s22} - i\omega\rho_s c_s = 0 \tag{34}$$

The coefficients E and F are found by substituting the particular solutions of the film and substrate into the respective differential equation:

$$E = \frac{\frac{P\alpha_f(1-R_f)}{2\pi}\exp\left(-\frac{\xi_1^2 a_1^2}{4} - \frac{\xi_2^2 a_2^2}{4}\right)}{k_{f33}\alpha_f^2 + 2\alpha_f\left(ik_{f13}\xi_1 + ik_{f23}\xi_2\right) - 2\xi_1\xi_2 k_{f12} - k_{f11}\xi_1^2 - k_{f22}\xi_2^2 - i\omega\rho_f c_f} \tag{35}$$

$$F = \frac{\frac{P\alpha_s(1-R_f)(1-R_s)\exp(-\alpha_f h)}{2\pi}\exp\left(-\xi_1^2\, a_1^2/_4 - \xi_2^2\, a_2^2/_4\right)}{k_{s33}\alpha_s^2 + 2\alpha_s(ik_{s31}\xi_1 + ik_{s32}\xi_2) - 2\xi_1\xi_2 k_{12} - k_{s11}\xi_1^2 - k_{s22}\xi_2^2 - i\omega\rho_s c_s} \tag{36}$$

The remaining coefficients A, B, and C are found by satisfying the boundary conditions. The transformed boundary conditions are given by

$$\left(-ik_{f31}\xi_1\hat{T}_f - ik_{f32}\xi_2\hat{T}_f + k_{f33}\hat{T}_{f,3}\right)|_{x_3=0} = 0 \tag{37}$$

$$\left(-ik_{f31}\xi_1\hat{T}_f - ik_{f32}\xi_2\hat{T}_f + k_{f33}\hat{T}_{f,3}\right)|_{x_3=h} = \left(-ik_{s31}\xi_1\hat{T}_s - ik_{s32}\xi_2\hat{T}_s + k_{s33}\hat{T}_{s,3}\right)|_{x_3=h} \tag{38}$$

$$-R_{th}\left(-ik_{f31}\xi_1\hat{T}_f - ik_{f32}\xi_2\hat{T}_f + k_{f33}\hat{T}_{f,3}\right)|_{x_3=h} = \left(T_f - T_s\right)|_{x_3=h} \tag{39}$$

Substituting the transformed solutions into the transformed boundary conditions gives the following system of equations

$$N \cdot \begin{bmatrix} A \\ B \\ C \end{bmatrix} = R \tag{40}$$

$$N_{11} = \left(-ik_{f31}\xi_1 - ik_{f32}\xi_2 - \eta_f k_{f33}\right) \tag{41}$$

$$N_{12} = \left(-ik_{f31}\xi_1 - ik_{f32}\xi_2 + \eta_f k_{f33}\right) \tag{42}$$

$$N_{13} = 0 \tag{43}$$

$$N_{21} = \left(-ik_{f31}\xi_1 - ik_{f32}\xi_2 - \eta_f k_{f33}\right)\exp\left(-\eta_f h\right) \tag{44}$$

$$N_{22} = \left(-ik_{f31}\xi_1 - ik_{f32}\xi_2 + \eta_f k_{f33}\right)\exp\left(-\eta_f h\right) \tag{45}$$

$$N_{23} = \left(ik_{f31}\xi_1 + ik_{f32}\xi_2 + \eta_f k_{f33}\right) \tag{46}$$

$$N_{31} = R_{th}\left(ik_{f31}\xi_1 + ik_{f32}\xi_2 + \eta_f k_{f33}\right)\exp\left(-\eta_f h\right) - \exp\left(-\eta_f h\right) \tag{47}$$

$$N_{32} = R_{th}\left(ik_{f31}\xi_1 + ik_{f32}\xi_2 - \eta_f k_{f33}\right)\exp\left(\eta_f h\right) - \exp\left(-\eta_f h\right) \tag{48}$$

$$N_{33} = 1 \tag{49}$$

$$R_1 = E\left(ik_{f31}\xi_1 + ik_{f32}\xi_2 + \alpha_f k_{f33}\right) \tag{50}$$

$$R_2 = E\left(ik_{f31}\xi_1 + ik_{f32}\xi_2 + \alpha_f k_{f33}\right)\exp\left(-\alpha_f h\right) - F(ik_{s31}\xi_1 + ik_{s32}\xi_2 + \alpha_s k_{s33}) \tag{51}$$

$$R_3 = E\left[1 - R_{Th}\left(ik_{f31}\xi_1 + ik_{f32}\xi_2 + \alpha_f k_{f33}\right)\right]\exp\left(-\alpha_f h\right) - F \tag{52}$$

Then an inverse Fourier transform is performed to find the equation for temperature.

Appendix C: BOM

Component	Price	Quantity
PHR-803t	$12.89	1
Aixiz IR laser	$35.00	1
Optical filters	$164.22	3
PDA36A	$327.42	1
Function Generator	$6.32	1
Lock-in Amplifier	$48.75	2
Arduino Mega	$35	1
Pickup Driver Circuit	$15	1
SR830 Lock-in Amplifier	$4150	1
Total	**$5123.04**	

Appendix D: Arduino Code

Main file:

```
#include "focus.h"


#include <SPI.h>
#include "AMIS30543.h"

// pins for chip select and motion
const uint8_t X_SS = 4; // This can change
const uint8_t x_stepPin = 5; // Fast High/Low only
const uint8_t x_dirPin = 6; // High/Low only
// Arduino pin 52 is the CLK so must be connected to any SPI peripherals
// SPI MISO pins are 50 and 1, but are not needed
// SPI MOSI pin is 51, will need to be connected to DI on driver

AMIS30543 stepper;

// endstop read
const int x_end = 2; // Needs to read only High vs Low

// Set up variables

// Current location
float x_location;
// micro step size
float MICRO = 128.0;
// new location
float x_new;
// distance needed to travel
float x_distance;
// number of steps needed
float x_turn;
// 20 full steps per rotation for this motor
float FullRotation = 20.0;
// set up end stop button
volatile int x_buttonState = LOW;
int n;
int xcheck;
int x_comp;
bool xdir; // useful to keep track of the current direction of motion
// direction is needed bc i think theres a gap that happens when changing direction



void setup()
{
  // put your setup code here, to run once:
  Serial.begin(9600);
  pinMode(FE, INPUT);
  pinMode(LS_PWR, OUTPUT);
  pinMode(LS_LNS, OUTPUT);
  pinMode(SEL1, OUTPUT);
  pinMode(SEL2, OUTPUT);
  pinMode(3, OUTPUT);
  pinMode(LS_LNS, OUTPUT);
  TCCR2A = _BV(COM2A1) | _BV(COM2B1) | _BV(WGM21) | _BV(WGM20); // see Fast PWM Mode at
https://www.arduino.cc/en/Tutorial/SecretsOfArduinoPWM
  TCCR2B = _BV(CS20); //no prescaler ie. x/1
  //SEL1 High, SEL2 Low - Red Laser
  //SEL1 Low, SEL2 High - IR Laser
  //SEL1 High, SEL2 High - UV Laser
  analogWrite(LS_PWR, 230);
  digitalWrite(SEL1, HIGH);
  digitalWrite(SEL2, HIGH);



  // set up serial input
  SPI.begin();
  SPI.beginTransaction(SPISettings(9600, MSBFIRST, SPI_MODE0));
  stepper.init(X_SS);

  // Drive the NXT/STEP and DIR pins low initially.
  digitalWrite(x_stepPin, LOW);
  pinMode(x_stepPin, OUTPUT);
  digitalWrite(x_dirPin, LOW);
```

```
  pinMode(x_dirPin, OUTPUT);
  digitalWrite(x_end, LOW);
  pinMode(x_end, INPUT);


  // Give the driver some time to power up.
  delay(10);

  // Reset the driver to its default settings.
  stepper.resetSettings();

  // Set the current limit.  You should change the number here to
  // an appropriate value for your particular system.
  stepper.setCurrentMilliamps(400);

  // Set the number of microsteps that correspond to one full step.
  stepper.setStepMode(MICRO);

  // Enable the motor outputs.
  stepper.enableDriver();

  SPI.endTransaction();
  //  // end SPI and begin normal Serial coms
  //  Serial.begin(9600);
  //  Serial.print("Ready to Zero");
  //  Serial.print("\n");
  //
  //  // Move forward 2 full rotations (6000 um) in case starting with button high
  //      Serial.print("Backing up");
  //      Serial.print("\n");
  //  for (int x=0;x<2*FullRotation*MICRO;x++){
  //      digitalWrite(x_dirPin,LOW); //rotation forward
  //      digitalWrite(x_stepPin,HIGH);
  //      delayMicroseconds(200);
  //      digitalWrite(x_stepPin,LOW);
  //      delayMicroseconds(1000);
  //      }
  //  delay(1000);
  //
  //
  //  /*
  //   * There is a function for the zeroing below
  //   * it moves the sled back until the pin is tripped to high
  //   * then forward until tripped to low
  //   * It shows that there is a gap between the screw and the teeth
  //   * this gap is important any time we change direction
  //   * UPDATE: maybe we don't need it?
  //   */
  //
  //  XZero();

  x_location = 0.00;


}

void loop()
{
  //  setDirection(HIGH);
  //  XMove(400);
  FocusLaser();
  int x = 1;

  //Modulates the IR Laser by incrementing the laser power up then down, f = ...
  //  for (int i = 75; i > 74; i = i + x) //move lens up and down once
  //  {
  //    int fe = analogRead(FE);
  //    analogWrite(LS_PWR,i);
  //    if (i == 100) x = -1;       //switch direction at peak https://www.arduino.cc/en/reference/for
  //    delay(10);
  //  }

  // delay(1000);

}

//Functions
/* set direction

*/
void setDirection(bool dir)
{
  // The NXT/STEP pin must not change for at least 0.5
```

```
  // microseconds before and after changing the DIR pin.
  delayMicroseconds(1);
  digitalWrite(x_dirPin, dir);
  delayMicroseconds(2);
}

/* X backwards motion

*/
float XBack(float x1, float x2) {
  float x_distance;
  float result;
  x_distance = x2 - x1;  // Make steps positive
  result = FullRotation * MICRO * x_distance / 3000.0; // Calculate number of steps needed
  //    digitalWrite(x_dirPin,HIGH); // Left hand rotation
  return result;
}

/* X forward motion

*/
float XForward(float x1, float x2) {
  float x_distance;
  float result;
  x_distance = x1 - x2;
  result = FullRotation * MICRO * x_distance / 3000.0; // Calculate number of steps needed
  //    digitalWrite(x_dirPin,LOW); //Right hand rotation
  return result;
}

/* X no motion

*/
float XStay() {
  float x_distance;
  float result;
  // Nothing done to x direction
  x_distance = 0.0;
  result = 0.0;
  return result;
}

/* X Zeroing

*/
float XZero() {
  float result;

  // move sled forawrd until button is triggered

  x_buttonState = digitalRead(x_end);
  Serial.print("Forward until button");
  Serial.print("\n");

  n = 0;
  while (n < 12 * FullRotation * MICRO) {

    x_buttonState = digitalRead(x_end);

    if (x_buttonState == LOW) {
      digitalWrite(x_dirPin, HIGH); //rotation backwards
      digitalWrite(x_stepPin, HIGH);
      delayMicroseconds(200);
      digitalWrite(x_stepPin, LOW);
      delayMicroseconds(1000);
      Serial.print("Step");
      Serial.println(n);
      Serial.print("\r");

    }

    if (x_buttonState == HIGH) {
      digitalWrite(x_stepPin, LOW);
      n = 12 * FullRotation * MICRO + 10;
      x_location = 0.0;
      Serial.print("Mess");
      Serial.print(n);
      Serial.print("\n");
    }
    n++;
    xdir = 1; // set direction
  }
  x_comp = 0;
```

```
  n = 0;

  /* I think there is a gap between the teeth of the black thing and the screw
     the sled responds decently when moving in the same direction as
     previous motion but there is a delay when changing directions

     I had measured it to be near 80 steps, but its always different
  */
  while (n < FullRotation * MICRO) {

    x_buttonState = digitalRead(x_end);

    if (x_buttonState == HIGH) {
      digitalWrite(x_dirPin, LOW); //rotation backwards
      digitalWrite(x_stepPin, HIGH);
      delayMicroseconds(200);
      digitalWrite(x_stepPin, LOW);
      delayMicroseconds(1000);
      x_comp = n;
      Serial.print("Compensation ");
      Serial.println(x_comp);
      Serial.print("\r");

    }

    if (x_buttonState == LOW) {
      digitalWrite(x_stepPin, LOW);
      n = 2 * FullRotation * MICRO + 10;
      x_location = 0.0;
      Serial.print("Done Compensation ");
      x_comp = x_comp - 15;  // for some reason x_comp is always a bit to big
      Serial.print(x_comp);
      Serial.print("\n");
    }
    n++;
    xdir = 0;
  }
  delay(100);
  Serial.print("X Location: Zeroed");
  Serial.print("\n");

  result = 0.0;
  return result;
}

/* X Move

*/
float XMove(float x1) {
  for (int x = 0; x < x1; x++) {
    digitalWrite(x_stepPin, HIGH);
    delayMicroseconds(20);
    digitalWrite(x_stepPin, LOW);
    delayMicroseconds(1000);
  }
}

/* Show when Done

*/
float XDone(float x1) {
  float result;
  // show when done
  Serial.print("X Done");
  Serial.print("\n");
  Serial.print("\n");
  // update current location
  result = x1;
  return result;
}
```

Focus.h

```
//Laser Diode Focusing
#define SEL1 12
#define SEL2 7
#define LS_PWR 8
#define LS_LNS 10
#define FE A3

void FocusLaser();
```

Focus.cpp

```
#include "focus.h"
#include "Arduino.h"

//function to get the focus position
void FocusLaser()
{
  int sensorMin = 1023;        // minimum sensor value
  int sensorMax = 0;           // maximum sensor value
  int x = 1;
  for (int i = 0; i > -1; i = i + x) //move lens up and down once
  {
    int fe = analogRead(FE);
    OCR2A = i;
    if (i == 255) x = -1;       //switch direction at peak https://www.arduino.cc/en/reference/for
    delay(5);

    // record the maximum sensor value see https://www.arduino.cc/en/Tutorial/Calibration
    if (fe > sensorMax) {
      sensorMax = fe;
    }

    // record the minimum sensor value
    if (fe < sensorMin) {
      sensorMin = fe;
    }
  }

  //if there isn't a max over a certain value generate an error

  //determine the amplitue of the S-curve
  int amp = sensorMax - sensorMin;

  //calculate a upper and lower acceptable postion for the laser to be focused see
http://www.diyouware.com/img/image037.jpg
  int fe_focus_position_pos = 506 + (amp / 16);
  int fe_focus_position_neg = 506 - (amp / 16);
  int motor_pwm_position_value = 0;

  delay(1000);
  x = 1;
  int i = 1;

  do    //do while loop, moves lens top to bottom while the fe signal is not equal to the upper or lower focus
limit(fe_focus_position_pos/neg)
  {
    int fe = analogRead(FE);

    OCR2A = i; //sets lens at top
    i = i + x;
    if (i % 255 == 1) i = 1;    //if its at the bottom it resets to top, ie. if i is divisible exactly by 255
it means the lens is at the bottom
    motor_pwm_position_value = i;
    delayMicroseconds(500);
          //  } while (analogRead(FE) > fe_focus_position_pos || analogRead(FE) < fe_focus_position_neg ||
analogRead(FE) < 510 || analogRead(FE) > 502);
  } while (analogRead(FE) != fe_focus_position_pos && analogRead(FE) != fe_focus_position_neg);   // more
consistent but takes longer
  OCR2A = motor_pwm_position_value;
//  OCR2A = 50; //130 neutral height
}
```

MotorControl.h

```
// Copyright Pololu Corporation.  For more information, see http://www.pololu.com/

/*! \file AMIS30543.h
 *
 * This is the main header file for the AMIS30543 library, a library for
 * controllering the AMIS-30543 micro-stepping stepper motor driver.
 *
 * For an overview of the features of this library, see
 *
 *   https://github.com/pololu/fastgpio-arduino
 *
 * That is the main repository for this library,
 *
 */

#pragma once

#include <stdint.h>
```

```
#include <Arduino.h>
#include <SPI.h>

/*! This class provides low-level functions for reading and writing from the SPI
 * interface of an AMIS-30543 micro-stepping stepper motor driver.
 *
 * Most users should use the AMIS30543 class, which provides a higher-level
 * interface, instead of this class. */
class AMIS30543SPI
{
public:

    /*! Configures this object to use the specified pin as a slave select pin.
     * You must use a slave select pin; the AMIS-30543 requires it. */
    void init(uint8_t slaveSelectPin) { ssPin = slaveSelectPin;

        digitalWrite(ssPin, HIGH);
        pinMode(ssPin, OUTPUT);
    }

    /*! Reads the register at the given address and returns its raw value. */
    uint8_t readReg(uint8_t address)
    {
        selectChip();
        transfer(address & 0b11111);
        uint8_t dataOut = transfer(0);
        deselectChip();
        return dataOut;
    }

    /*! Writes the specified value to a register. */
    void writeReg(uint8_t address, uint8_t value)
    {
        selectChip();
        transfer(0x80 | (address & 0b11111));
        transfer(value);

        // The CS line must go high after writing for the value to actually take
        // effect.
        deselectChip();
    }

private:

    SPISettings settings = SPISettings(9600, MSBFIRST, SPI_MODE0);

    uint8_t transfer(uint8_t value)
    {
        return SPI.transfer(value);
    }

    void selectChip()
    {
        digitalWrite(ssPin, LOW);
        SPI.beginTransaction(settings);
    }

    void deselectChip()
    {
       digitalWrite(ssPin, HIGH);
       SPI.endTransaction();

       // The CS high time is specified as 2.5 us in the AMIS-30543 datasheet.
       delayMicroseconds(3);
    }

    uint8_t ssPin;
};

/*! This class provides high-level functions for controlling an AMIS-30543
 *  micro-stepping motor driver.
 *
 * It provides access to all the features of the AMIS-30543 SPI interface
 * except the watchdog timer. */
class AMIS30543
{
public:
    /*! The default constructor. */
    AMIS30543()
    {
        wr = cr0 = cr1 = cr2 = cr3 = 0;
    }
```

```
/*! Possible arguments to setStepMode(). */
enum stepMode
{
    MicroStep128 = 128,
    MicroStep64 = 64,
    MicroStep32 = 32,
    MicroStep16 = 16,
    MicroStep8 = 8,
    MicroStep4 = 4,
    MicroStep2 = 2,
    MicroStep1 = 1,
    CompensatedHalf = MicroStep2,
    CompensatedFullTwoPhaseOn = MicroStep1,
    CompensatedFullOnePhaseOn = 200,
    UncompensatedHalf = 201,
    UncompensatedFull = 202,
};

/*! Bitmasks for the return value of readNonLatchedStatusFlags(). */
enum nonLatchedStatusFlag
{
    OPENY = (1 << 2),
    OPENX = (1 << 3),
    WD = (1 << 4),
    CPFAIL = (1 << 5),
    TW = (1 << 6),
};

/*! Bitmasks for the return value of readLatchedStatusFlagsAndClear(). */
enum latchedStatusFlag
{
    OVCXNB = (1 << 3),
    OVCXNT = (1 << 4),
    OVCXPB = (1 << 5),
    OVCXPT = (1 << 6),
    TSD = (1 << 10),
    OVCYNB = (1 << 11),
    OVCYNT = (1 << 12),
    OVCYPB = (1 << 13),
    OVCYPT = (1 << 14),
};

/*! Addresses of control and status registers. */
enum regAddr
{
    WR  = 0x0,
    CR0 = 0x1,
    CR1 = 0x2,
    CR2 = 0x3,
    CR3 = 0x9,
    SR0 = 0x4,
    SR1 = 0x5,
    SR2 = 0x6,
    SR3 = 0x7,
    SR4 = 0xA,
};

/*! Configures this object to use the specified pin as a slave select pin.
 * You must use a slave select pin; the AMIS-30543 requires it. */
void init(uint8_t slaveSelectPin)
{
    driver.init(slaveSelectPin);
}

/*! Changes all of the driver's settings back to their default values.
 *
 * It is good to call this near the beginning of your program to ensure that
 * There are no settings left over from an earlier time that might affect the
 * operation of the driver. */
void resetSettings()
{
    wr = cr0 = cr1 = cr2 = cr3 = 0;
    applySettings();
}

/*! Reads back all the SPI control registers from the device and
 * verifies that they are equal to the cached copies stored in this class.
 *
 * This can be used to verify that the driver is powered on and has not lost
 * them due to a power failure.  However this function will probably return
 * true if the driver is not powered and all of the cached settings are the
 * default values.  Therefore, we only recommend calling this after you have
 * changed at least one of the settings from its default value, for example
```

```
 * by calling enableDriver().
 *
 * @return 1 if the settings from the device match the cached copies, 0 if
 * they do not. */
bool verifySettings()
{
    return driver.readReg(WR) == wr &&
        driver.readReg(CR0) == cr0 &&
        driver.readReg(CR1) == cr1 &&
        driver.readReg(CR2) == cr2 &&
        driver.readReg(CR3) == cr3;
}

/*! Re-writes the cached settings stored in this class to the device.
 *
 * You should not normally need to call this function because settings are
 * written to the device whenever they are changed.  However, if
 * verifySettings() returns false (due to a power interruption, for
 * instance), then you could use applySettings to get the device's settings
 * back into the desired state. */
void applySettings()
{
    // Because of power interruption considerations, the register that
    // contains the MOTEN bit (CR2) must be written first, and whenever we
    // write to it we should also write to all the other registers.

    // CR2 is written first, because it contains the MOTEN bit, and there is
    // a risk that there might be a power interruption to the driver right
    // before CR2 is written.  This could result in the motor being enabled
    // with incorrect settings.  Also, whenever we do write to CR2, we want to
    // also write the other registers to make sure they are in the correct state.
    driver.writeReg(CR2, cr2);

    writeWR();
    writeCR0();
    writeCR1();
    writeCR3();
}

/*! Sets the MOTEN bit to 1, enabling the driver.
 *
 * Please read the note about this function in README.md. */
void enableDriver()
{
    cr2 |= 0b10000000;
    applySettings();
}

/*! Sets the MOTEN bit to 0, disabling the driver.
 *
 * Please read the note about this function in README.md. */
void disableDriver()
{
    cr2 &= ~0b10000000;
    applySettings();
}

/*! Sets the per-coil current limit equal to the highest available setting
 * that is less than the given current, in units of milliamps.
 *
 * Refer to Table 13 of the AMIS 30543 datasheet to see which current limits
 * are available. */
void setCurrentMilliamps(uint16_t current)
{
    // This comes from Table 13 of the AMIS-30543 datasheet.
    uint8_t code = 0;
     %uncomment
    if      (current >= 3000) ( code = 0b11001; )
    else if (current >= 2845) ( code = 0b11000; )
    else if (current >= 2700) ( code = 0b10111; )
    else if (current >= 2440) ( code = 0b10110; )
    else if (current >= 2240) ( code = 0b10101; )
    else if (current >= 2070) ( code = 0b10100; )
    else if (current >= 1850) { code = 0b10011; )
    else if (current >= 1695) ( code = 0b10010; )
    else if (current >= 1520) ( code = 0b10001; )
    else if (current >= 1405) ( code = 0b10000; )
    else if (current >= 1260) ( code = 0b01111; )
    else if (current >= 1150) ( code = 0b01110; )
    else if (current >= 1060) ( code = 0b01101; )
    else if (current >=  955) ( code = 0b01100; )
    else if (current >=  870) ( code = 0b01011; )
    else if (current >=  780) ( code = 0b01010; )
```

```
    else if (current >=  715) ( code = 0b01001; )
    else if (current >=  640) ( code = 0b01000; )
    else if (current >=  585) ( code = 0b00111; )
    else if (current >=  540) ( code = 0b00110; )
    else if (current >=  485) ( code = 0b00101; )
    else if (current >=  445) ( code = 0b00100; )
    else if (current >=  395) ( code = 0b00011; )
    else if (current >=  355) ( code = 0b00010; )
    else if (current >=  245) ( code = 0b00001; )

    cr0 = (cr0 & 0b11100000) | code;
    writeCR0();
}

/*! Reads the current microstepping position, which is a number between 0
 * and 511.
 *
 * The different positions and their corresponding coil values are listed in
 * Table 9 of the AMIS 30543 datasheet.
 *
 * The lower two bits of this return value might be inaccurate if the step
 * pin is being toggled while this function runs (e.g. from an interrupt or
 * a PWM signal).
 *
 * Our tests indicated that the return value of this function might be wrong
 * if you read it within 25 microseconds of commanding the driver to take a
 * step.  Therefore we recommend delaying for at least 100 microseconds after
 * taking a step and before calling this function. */
uint16_t readPosition()
{
    uint8_t sr3 = readStatusReg(SR3);
    uint8_t sr4 = readStatusReg(SR4);
    return ((uint16_t)sr3 << 2) | (sr4 & 3);
}

/*! Sets the value of the DIRCTRL configuration bit.
 *
 * Allowed values are 0 or 1.
 *
 * You can use this command to control the direction of the stepper motor
 * and simply leave the DIR pin disconnected. */
void setDirection(bool value)
{
    if (value)
    {
        cr1 |= 0x80;
    }
    else
    {
        cr1 &= ~0x80;
    }
    writeCR1();
}

/*! Returns the cached value of the DIRCTRL configuration bit.
 *
 * This does not perform any SPI communication with the driver. */
bool getDirection()
{
    return cr1 >> 7 & 1;
}

/*! Configures the driver to have the specified stepping mode.
 *
 * This affects many things about the performance of the motor, including
 * how much the output moves for each step taken and how much current flows
 * through the coils in each stepping position.
 *
 * If an invalid stepping mode is passed to this function, then it selects
 * 1/32 micro-step, which is the driver's default. */
void setStepMode(uint8_t mode)
{
    // Pick 1/32 micro-step by default.
    uint8_t esm = 0b000;
    uint8_t sm = 0b000;

    // The order of these cases matches the order in Table 12 of the
    // AMIS-30543 datasheet.
    switch(mode)
    {
    case MicroStep32: sm = 0b000; break;
    case MicroStep16: sm = 0b001; break;
    case MicroStep8: sm = 0b010; break;
```

```
    case MicroStep4: sm = 0b011; break;
    case CompensatedHalf: sm = 0b100; break; /* a.k.a. MicroStep2 */
    case UncompensatedHalf: sm = 0b101; break;
    case UncompensatedFull: sm = 0b110; break;
    case MicroStep128: esm = 0b001; break;
    case MicroStep64: esm = 0b010; break;
    case CompensatedFullTwoPhaseOn: esm = 0b011; break;  /* a.k.a. MicroStep 1 */
    case CompensatedFullOnePhaseOn: esm = 0b100; break;
    }

    cr0 = (cr0 & ~0b11100000) | (sm << 5);
    cr3 = (cr3 & ~0b111) | esm;
    writeCR0();
    writeCR3();
}

/*! Sets the SLP bit 1, enabling sleep mode.
 *
 * According to the AMIS-30543 datasheet, the motor supply voltage must be
 * at least 9 V before entering sleep mode.
 *
 * You can call sleepStop() to disable sleep mode.
 *
 * Please read the note about this function in README.md. */
void sleep()
{
    cr2 |= (1 << 6);
    applySettings();
}

/*! Sets the SLP bit 0, disabling sleep mode.
 *
 * Please read the note about this function in README.md. */
void sleepStop()
{
    cr2 &= ~(1 << 6);
    applySettings();
}

/*! Sets the value of the NXTP configuration bit to 0, which means that new
 * steps are triggered by a rising edge on the NXT/STEP pin.  This is the
 * default behavior. */
void stepOnRisingEdge()
{
    cr1 &= ~0b01000000;
    writeCR1();
}

/*! Sets the value of the NXTP configuration bit to 1, which means that new
 * steps are triggered by a falling edge on the NXT/STEP pin. */
void stepOnFallingEdge()
{
    cr1 |= 0b01000000;
    writeCR1();
}

/*! Sets the PWMF bit to 1, which doubles the PWM frequency (45.6 kHz) .*/
void setPwmFrequencyDouble()
{
    cr1 |= (1 << 3);
    writeCR1();
}

/*! Clears the PWMF bit, which sets the PWM frequency to its default value
 *  (22.8 kHz). */
void setPwmFrequencyDefault()
{
    cr1 &= ~(1 << 3);
    writeCR1();
}

/*! Sets the PWMJ bit, which enables artificial jittering in the PWM signal
 *  used to control the current to each coil. */
void setPwmJitterOn()
{
    cr1 |= (1 << 2);
    writeCR1();
}

/*! Clears the PWMJ bit, which disables artificial jittering in the PWM
 *  signal used to control the current to each coil.  This is the default
 *  setting. */
void setPwmJitterOff()
```

```
{
    cr1 &= ~(1 << 2);
    writeCR1();
}

/*! This sets the EMC[1:0] bits, which determine how long it takes the PWM
 *  signal to rise or fall.  Valid values are 0 through 3.  Higher values
 *  correspond to longer rise and fall times.  **/
void setPwmSlope(uint8_t emc)
{
    cr1 = (cr1 & ~0b11) | (emc & 0b11);
    writeCR1();
}

/*! Clears the SLAG bit, which configures the signal on SLA pin to have a
 *  gain of 0.5 (the default).
 *
 * Please read the note about this function in README.md. */
void setSlaGainDefault()
{
    cr2 &= ~(1 << 5);
    applySettings();
}

/*! Sets the SLAG bit to 1, which configures the signal on SLA pin to have a
 *  gain of 0.25 (half of the default).
 *
 * Please read the note about this function in README.md. */
void setSlaGainHalf()
{
    cr2 |= (1 << 5);
    applySettings();
}

/*! Set the SLAT bit to 0 (the default), which disables transparency on the
 *  SLA pin.  See the AMIS-30543 datasheet for more information.
 *
 * Please read the note about this function in README.md. */
void setSlaTransparencyOff()
{
    cr2 &= ~(1 << 4);
    applySettings();
}

/*! Sets the SLAT bit to 1, which enables transparency on the SLA pin.
 *  See the AMIS-30543 datasheet for more information.
 *
 * Please read the note about this function in README.md. */
void setSlaTransparencyOn()
{
    cr2 |= (1 << 4);
    applySettings();
}

/*! Reads the status flags from registers SR0.  These flags are not latched,
 * which means they will be cleared as soon as the condition causing them is
 * no longer detected.  See the AMIS-30543 datasheet for more information.
 *
 * This function returns the raw value of SR0, with the parity bit set to 0.
 * You can simply compare the return value to 0 to see if any of the status
 * flags are set, or you can use the logical AND operator (`&`) and the
 * #nonLatchedStatusFlag enum to check individual flags.
 *
 * ~~~~(.cpp)
 * uint16_t flags = stepper.readNonLatchedStatusFlags();
 * if (flags)
 * {
 *   // At least one flag is set.
 *
 *   if (flags & AMIS30543::OPENX)
 *   {
 *     // Thermal shutdown flag is set.
 *   }
 *
 * }
 * ~~~~
 */
uint16_t readNonLatchedStatusFlags()
{
    return readStatusReg(SR0);
}

/*! Reads the latched status flags from registers SR1 and SR2.  They are
```

```
     *  cleared as a side effect.
     *
     * The return value is a 16-bit unsigned integer that has one bit for each
     * status flag.  You can simply compare the return value to 0 to see if any
     * of the status flags are set, or you can use the logical and operator (`&`)
     * and the #latchedStatusFlag enum to check individual flags.
     *
     * WARNING: Calling this function clears the latched error bits in SR1 and
     * SR2, which might allow the motor driver outputs to reactivate.  The
     * AMIS-30543 datasheet says "successive reading the SPI Status Registers 1
     * and 2 in case of a short circuit condition, may lead to damage to the
     * drivers". */
    uint16_t readLatchedStatusFlagsAndClear()
    {
        uint8_t sr1 = readStatusReg(SR1);
        uint8_t sr2 = readStatusReg(SR2);
        return (sr2 << 8) | sr1;
    }

protected:

    uint8_t wr, cr0, cr1, cr2, cr3;

    /*! Reads a status register and returns the lower 7 bits (the parity bit is
     *  set to 0 in the return value). */
    uint8_t readStatusReg(uint8_t address)
    {
        // Mask off the parity bit.
        // (Later we might add code here to check the parity
        // bit and record errors.)
        return driver.readReg(address) & 0x7F;
    }

    /*! Writes the cached value of the WR register to the device. */
    void writeWR()
    {
        driver.writeReg(WR, wr);
    }

    /*! Writes the cached value of the CR0 register to the device. */
    void writeCR0()
    {
        driver.writeReg(CR0, cr0);
    }

    /*! Writes the cached value of the CR1 register to the device. */
    void writeCR1()
    {
        driver.writeReg(CR1, cr1);
    }

    /*! Writes the cached value of the CR3 register to the device. */
    void writeCR3()
    {
        driver.writeReg(CR3, cr3);
    }

public:
    /*! This object handles all the communication with the AMIS-30543.  It is
     * only marked as public for the purpose of testing this library; you should
     * not use it in your code. */
    AMIS30543SPI driver;
};
```

Appendix E: How to Collect and Analyze Data

Blu-ray Data Collection Process

1. Wire it up. Function generator to lock in and IR. Photodiode to lock-in. Lock-in to computer.
2. Turn on everything. There are 6 things to turn on including the Arduino
    a. Power supply
    b. Lock in
    c. Photodiode power supply
    d. Photodiode
    e. Function generator
    f. Arduino
3. Set up function generator
    a. Hi level: 3.3V, low level: 2V
4. Open Matlab data acquisition program: J:\groups\munroresearc\Data\Blu-Ray Project\SR830_data_acquisition
5. Unlock lock in so it is referencing function generator, not itself
6. Name file in frequency box, it saves to where the data acquisition file is saved
    a. Image of file name box

Curve Fitting Data with Fitmain.m

1. Open fitmain located in J:\groups\munroresearc\Programs\MATLAB\Christ_codes
2. This will open:

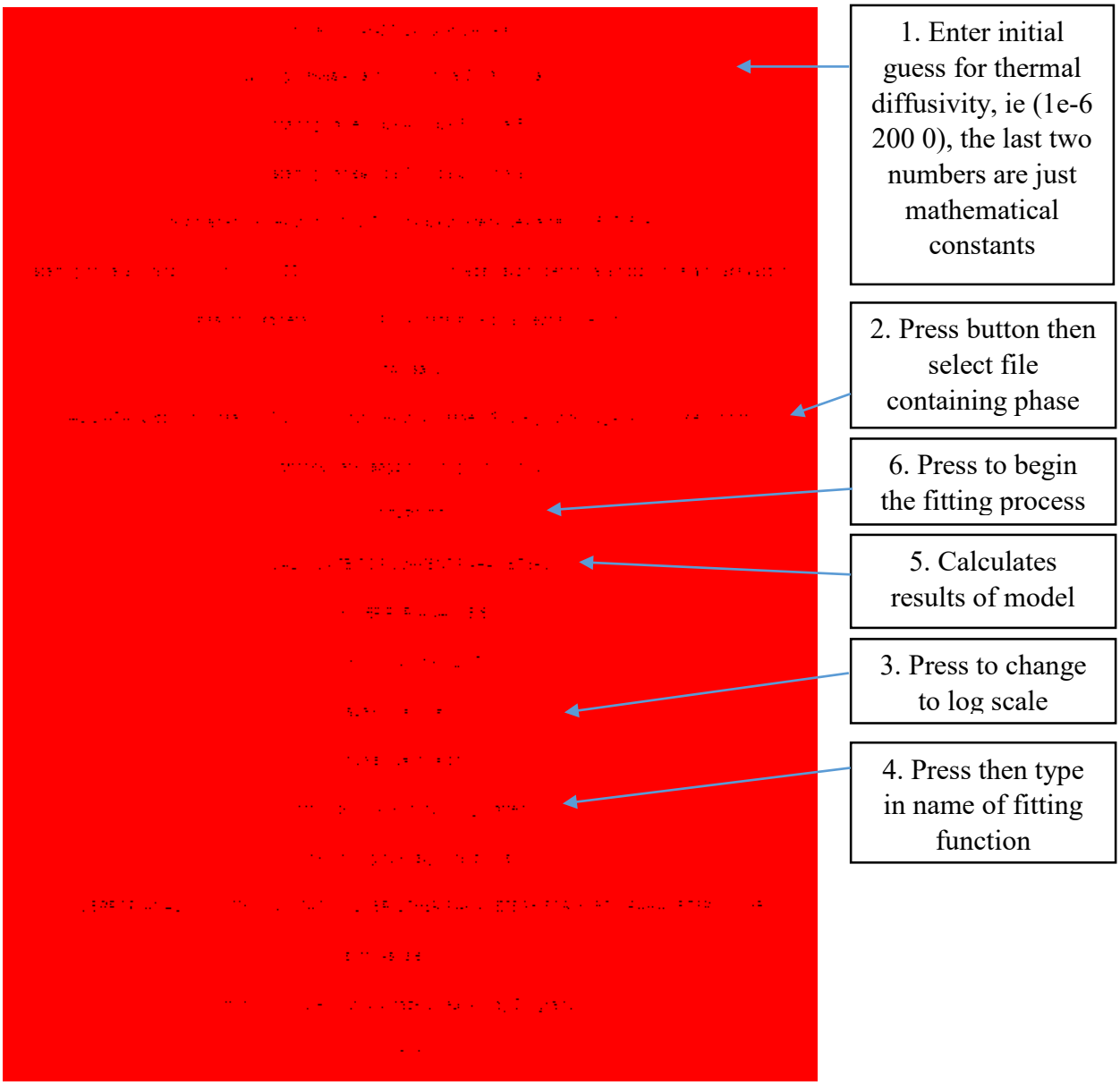

   a. Data should be in the following format: frequency (Hz), phase delay (degrees)

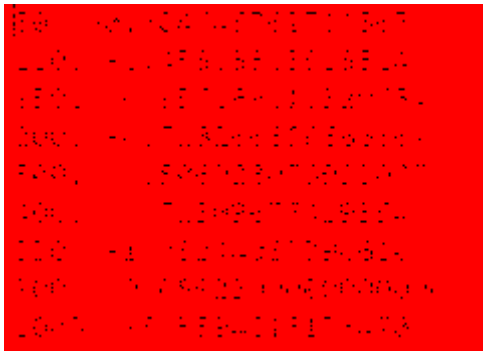

3. After it runs, the best fit parameters box will list the thermal diffusivity as the first parameter